МИНИСТЕРСТВО ОБРАЗОВАНИЯ И НАУКИ РОССИЙСКОЙ ФЕДЕРАЦИИ

федеральное государственное бюджетное образовательное учреждение

высшего образования

«РОССИЙСКИЙ ГОСУДАРСТВЕННЫЙ

ГИДРОМЕТЕОРОЛОГИЧЕСКИЙ УНИВЕРСИТЕТ»

Кафедра ДАКЗ

ВЫПУСКНАЯКВАЛИФИКАЦИОННАЯРАБОТА

НатемуDetection of fog and low stratus clouds in the Arctic zone using multispectral imagery

Исполнитель Таций Дарья Владимировна

(фамилия, имя, отчество)

Руководитель ___*Доцент, Канд. геогр. наук*___

(ученая степень, ученое звание)

Федосеева Наталья Владимировна

(фамилия, имя, отчество)

«К защите допускаю»

Заведующийкафедрой_____

(подпись)

Доцент, Канд. физ.-мат. Наук

(ученая степень, ученое звание)

Егоров_Кирилл Леонидович

(фамилия, имя, отчество)

«___»_____20__г.

Санкт–Петербург

2017

Content

Reductions

SST – Sea Surface Temperature

MODIS - Moderate Resolution Imaging Spectroradiometer

EOS – Earth Observation System

AVHRR - Advanced very-high-resolution radiometer

NOAA - National Oceanic and Atmospheric Administration

NASA - National Aeronautics and Space Administration

CTD – Coastal trapped disturbance

PDO - Pacific Decadal Oscillation

ENSO - El Niño Southern Oscillation

GOES – Geostationary Operational Environmental Satellite

FLS – Fog and Low Stratus

SEVIRI - Spinning Enhanced Visible and Infrared Imager

MISR – Multi-angle Imaging SpectroRadiometer

CERES – Capacité de REnseignement Electromagnétique Spatial

HIRS – High-resolution Infrared Radiation Sounder

MAS – MODIS Airborne Simulator

NCEP – National Centers for Environmental Prediction

DAO – Data Assimilation Office

LWP – Liquid water path

Introduction

Fog is a phenomenon, impacting on air quality, traffic safety and the climate system. Fog detection with good spatial and temporal resolution therefore is of great interest to applications in these fields. Ground station data do not yield a spatially coherent picture of the fog distribution. Satellite data on the other hand is ideally suited to fulfil all requirements. The results of work presented here have led to the development of new techniques for the detection of low stratus and surface fog from satellite data only.

The importance of prompt detection and recognizing of fog and low stratus clouds in images with snow and ice cover or cloudiness of the upper and or middle layer in order to ensure the safe operation of aircraft and ships, particularly in areas of insufficient coverage of automatic meteorological stations requires the qualitative analysis of satellite images.

The project deals with the problem of interpretation of images obtained from satellites Aqua and Terra with a scanning radiometer MODIS in 36 spectral ranges, with wavelengths from 0.4 µm to 14.4 µm and a resolution from 250 m to 1 km. Aqua and Terra satellite systems, included to the EOS program, have been created for monitoring of the global dynamics of our planet.

With the program Beam VISAT 5.0, designed to work with satellite data in raster format, thematic digital techniques of satellite multispectral information, based on difference images, both in optical and far-infrared ranges of the spectrum, have been developed to improve the quality of interpretation of fogs and low stratus clouds in terms of the complex structure of cloudiness and underlying surface.

Chapter 1. Aspects of fog formation

1.1 Climate Influences on Arctic Weather

Arctic weather is influenced by several factors, many of which are not found at lower latitudes.

1. Continuous daylight at the height of summer followed by continuous darkness in the depths of winter. Combined with the sun's low height above the horizon, this leads to heavy radiative heat loss through much of the year;

2. The presence of snow and sea ice on the surface for much of the year reflects much of the incoming shortwave solar radiation;

3. Sea ice cover on the ocean limits the amount of available moisture that can be picked up and carried by the atmosphere. Cool surface air temperatures further limit the humidity.

4. There are relatively few mountains at high latitudes to obstruct atmospheric flow between mid latitudes and the Arctic. The areas of highest relief are Greenland, Ellesmere and Baffin Islands in Canada, the Brooks and Alaska ranges in Alaska, and the mountains of Scandinavia. Thus, weather is dominated by synoptic systems rather than mesoscale features.[1]

1.2 Synoptic Patterns

The synoptic picture of the Arctic is dominated by only a few features. In winter we find lows over the North Atlantic (Icelandic Low) and North Pacific (Aleutian Low). These lows are separated by a ridge composed of the intense Siberian High and the weaker Beaufort and North American Highs. It is important

to understand that the Aleutian and Icelandic Lows are climatological features reflecting the high frequency of lows in the area. On a day-to-day basis these lows can be located anywhere across a broad region. The Siberian High is an intense, shallow, cold anticyclone that forms in response to radiational cooling over eastern Siberia in winter. It is associated with frequent cold air outbreaks over East Asia.

In summer, the Siberian High is replaced by a thermal low. The Aleutian and Icelandic Lows nearly disappear as the frequency of cyclones in the northern oceans drops considerably.

1.2.1 Polar Vortex
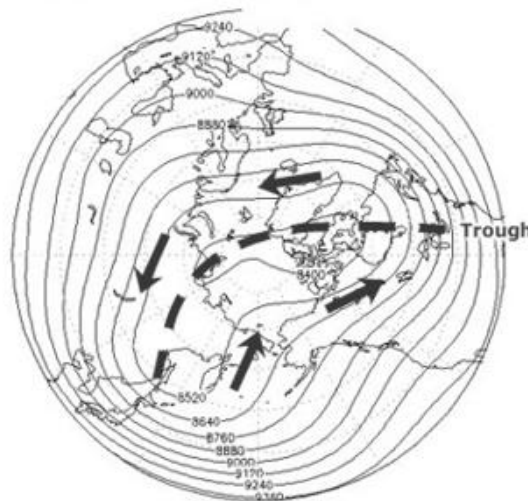
Figure 1. Mean 300-mb Heights for January, 1958-2005, based on NCEP/NCAR Reanalysis [1].

Heights of pressure surfaces are much lower in the Arctic than at mid latitudes. This results in a persistent large-scale, cyclonic circulation pattern in the middle and upper troposphere called the polar vortex. This feature is present over both the north and south poles. In the Arctic, the vortex is rather elongate with troughs over eastern North America and eastern Asia. As we have seen earlier, the

polar vortex is not present at the surface; rather, it becomes a coherent feature only at about 500 mb and higher.

1.2.2 Tropopause

Figure 2. Representative Winter and Summer soundings from Franz Josef Land in the High Arctic (80N, 58E). 00 UTC 05 Jan 2010 (left) and 12 UTC 11 Jun 2010 (right) [1].
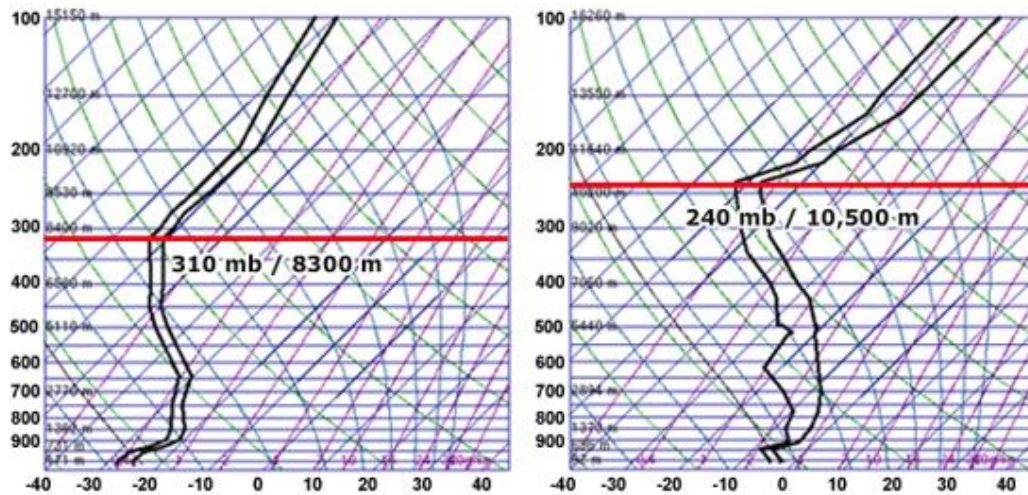
Generally speaking, in the Arctic, the tropopause (the level at which the fall of temperature with height ceases) is lower than in the tropics. The height of the tropopause changes regularly in the Arctic from 8000 m in January to more than 10,000 m in July. These soundings originated from Franz Josef Arrive in the high Arctic (80N). The tropopause on 5 January was at around 310 mb or 8300 m. On 11 June, it was around 240 mb or 10,500 m.

If we look at maps of the height of the tropopause, we see a solid angle in the mid latitudes that shifts north in the late spring and south in the winter. This angle denote the area of the polar jet.

Accordingly of the lower tropopause, clouds and storms are for the most part lower in the Arctic than at mid latitudes. In winter even exceptional cyclones are

generally kept to heights underneath 15,000 ft (4600 m). The uncommon thunderstorm might be topped at a comparable level.

1.2.3 Seasonal Temperatures

Ashore, temperatures in the Arctic are very factor. Outside of glaciated regions, snow cover is very thin and melts ahead of schedule in summer. This enables land to warm impressively under the ceaseless sunlight. Be that as it may, under the constant dimness of winter, land cools and temperatures can turn out to be intensely frosty.

Over the sea, summer temperatures are emphatically directed by untamed water and ocean ice, which have summer temperatures almost 0°C. In the winter, the water in the Arctic ocean underneath the polar ice pack is never colder than -2°C (28°F). This conservatives keeps Arctic winters hotter than those in Antarctica.

The coldest winter temperatures ordinarily happen in northern Asia, while the hottest winter temperatures are found where the North Atlantic current streams up into the Norwegian and Barents Seas.
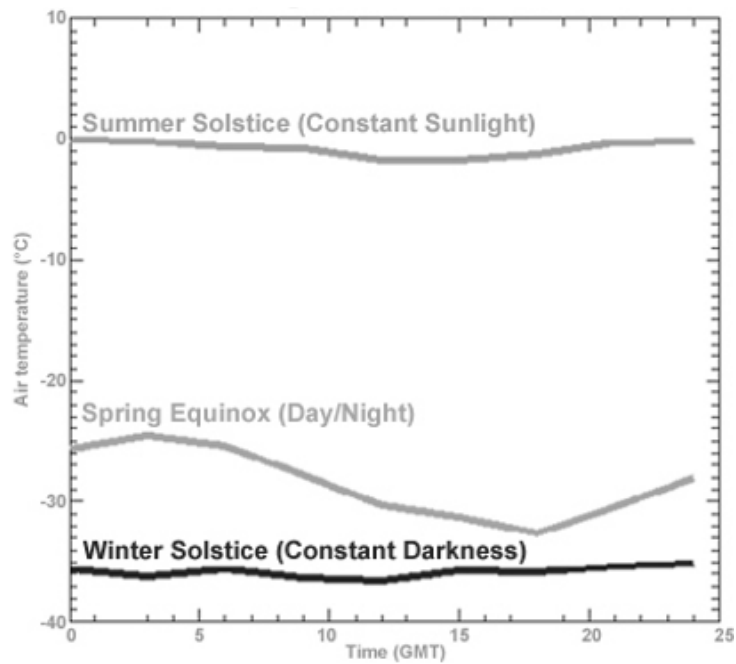
Figure 3. Surface air temperature over the course of the day, from drifting station NP-30, North of 75°N [1].

Continuous daytime in summer and obscurity in winter prompt temperatures without a diurnal cycle of daytime warming and evening cooling. In winter, clear skies prompt solid radiational cooling and the development of inversions. Temperatures rise when winds are sufficiently solid to blend out the reversal and convey warm air up high down to the surface. Cyclones bring not just high winds that blend out the reversal, additionally draw warmer, moister air from lower latitudes.

Cyclones in Arctic present a huge gauge challenge, bringing precipitation, high winds, and high oceans. Violent winds can likewise prompt warming, by either bringing warm air from the south or by blending out the wintertime inversion. Visibility is lessened when warm, humid air is advected over frosty SSTs or ocean ice, bringing about broad fog or low stratus. Cyclones incited strong winds can prompt blowing snow, which likewise decreases visibility.

1.2.4 Precipitation

Precipitation sums in Arctic differ generally. Where the warm North Atlantic current passes Greenland and enters the Norwegian and Barents seas, precipitation ranges from 400 to more than 1000 mm/yr (16-40 inches). Over the Beaufort Sea and Northern Greenland, precipitation midpoints as meager as 150 mm/yr (6 inches). Whatever is left of Arctic falls between these extremes with mainland zones being more humid than sea territories.

In winter, far from the untamed waters of the North Atlantic, there is little moisture accessible for precipitation. Snow and ice cover joined with cool temperatures keep moisture low. Subsequently, overwhelming snowfall is not basic in Arctic and uncommonly substantial snowfalls are confined to precipitous and sea ranges.

1.2.5 Wind

In winter, surface wind speeds have a tendency to be lower than one may expect given the lack of trees and mountains. This happens on the grounds that the inversion that rules winter climate decouples the surface wind from more grounded winds high up. Additionally seaside temperature inclinations are weaker in the winter than summer, because of the nearness of ocean ice instead of untamed water.

In summer, inversions are less stronger and weaker. Besides, long days dissolve ocean ice and warm the land, which expands the temperature differentiate crosswise over seaside zones. This prompts more incessant cyclones and higher coastal front winds. Therefore, surface winds increment in the mid year [1, 2].

1.3 Types of fog

Arctic climate stations encounter fog conditions on the request of 100 days for each year, for the most part in summer. Over the cool water of the Arctic ocean, fog happens often, especially amid the late spring months when waters are without ice. All through the Arctic, fog and low stratus happens in most cases in June and July.

Fog happens most habitually along the seaside zones, commonly in a belt parallel to the shore where solid flat temperature and moisture angles exist between ice, water, and land. The high recurrence of event for fog specifically influences intensely used shipping lanes from the Atlantic into the Norwegian and Greenland seas. Also, the vast waters of the Kara, Laptev, East Siberian, and Chukchi seas are especially helpful for summer fog or low stratus cloud arrangement. Amid a commonplace summer, these zones may encounter fog 15 to 20 days for each month. The Bering sea is additionally influenced by late spring fog and stratus, as southerly stream brings warm, moist air northward. In a few ranges of Arctic, upwards of 80 to 95% of summer days can be cloudy, making the Arctic one of the cloudiest locales in the Northern Hemisphere of the planet. In the winter, fog is more probable over the neighboring area regions, which can wind up noticeably colder than the ice-secured sea.

Winter additionally brings the danger of ice fog, made out of moment ice crystals, and steam fog, a phenomenon that happens when the air temperatures are essentially colder than the water temperature. Steam fog, otherwise called sea smoke, happens over vast water, incorporating leads or sections in the ice pack. Amid times of the year where some sunlight is available, fog will more often than not happen during the early morning and evening time hours. The districts flanking the East Siberian and Laptev sea show an exemption. Here fog happens is most

prominent around midnight. At twelve the fog probability is slightest. Low-level blending in the limit layer over the Barents and Norwegian seas makes these zones the minimum foggy in summer.

Fog can be caused by a number of different mechanisms. Knowledge of these mechanisms aids the forecaster in anticipating the likely occurrence of fog at various locations. The four main fog types are:

1.3.1 Advection Fog

Advection fog forms in summer when warm, moist air flows over the melting pack ice and cold open water. High wind rates will regularly make the fog lift, bringing about low stratus. Advection fog is typically inconsistent and keeps going just a moderately brief time. June and July are the times of most elevated likelihood of that type of fog. Advection fog—colder air flowing over a warmer sea (warm sea fog or warm fog). Another concept of fog formation stems from advection of colder air over the warm sea where saturation occurs in response to mixing of the cold and sufficiently moist air with warm/moist air.

1.3.2 Radiation Fog

Radiation fog happens most oftentimes with clear, quiet conditions over snow and additionally ice covers. The surface layer of air is cooled by active radiation amid the night, temperatures are decreased to the dew point, and buildup happens. These fogs can happen over the pack ice, however they are most oftentimes found along waterway valleys where air development is insignificant and waste renders the air very icy. They are most regular in the lower Lena and Mackenzie Waterway Valleys. Radiation fogs may likewise happen in the Yukon

Valley and in a portion of the valleys of northward streaming waterways in Siberia. Radiation fogs are by and large thin and shallow and consume off in the daytime. In the lower Mackenzie 20-25 mist days may happen in a month.

The radiation fog is likewise a decent pointer of a solid low-level inversion that hinders vertical mixing. As might be normal, radiation fogs are most regular in fall and early winter.

1.3.3 Steam Fog

Steam fog happens when exceptionally icy, dry air comes into contact with a moderately warm water surface (leads, polynyi, and so on.), bringing on a fast exchange of warmth and moisture from the water surface to the air. The heating from below produces an unstable lapse rate, and associated small scale convective eddies carry the warm, moist surface air aloft where it mixes with the colder, dryer air above. Buildup happens as fog, however with further mixing of the dry air the fog will break down. Steam fog is at times alluded to as Arctic sea smoke.

Steam fog—advected air significantly colder than the ocean. At the point when a surge of frosty, dry air (commonly beginning over land) crosses a significantly warmer ocean surface, a "steam fog" can happen. Such occasions additionally happen with consistency over lakes in wintertime. The huge warmth limit of water prompts slower cooling of the lake water in respect to the land mass (particularly striking in late fall and early winter). In both cases, i.e., over lakes or seas, the idle and sensible warmth fluxes are outrageous (regularly achieving estimations of at least 100s of W m−2 for both sensible and inert warmth fluxes). The steam fog is every now and again seen in the Arctic zone. Further observations and simulations, particularly for instances of bigger air–sea temperature contrasts, are expected to uncover the part of SST in steam fog.

1.3.4 Ice Fog

The fogs mentioned previously are usually water fogs. Ice fog happens amid the winter when a lot of water are added to a great degree cool air (- 30 °C). The subsequent light ice particles (crystals) settle gradually and in this manner stay suspended noticeable all around for drawn out stretches of time. These ice fogs are regular around possessed territories where an assortment of moisture sources can be found. Amid the Planned Eastern Cold Investigation (CEAREX) in the MIZ, a mellow form of ice fog, which had little effect on visibility however which was quite often clear, was named to as "diamond dust."

1.3.5. Clouds

As in other parts of the world, Arctic clouds are produced by one of several cooling mechanisms:

1. Dynamic lifting in low pressure systems or at convergence lines and fronts;
2. Radiational cooling, which is responsible normally for low clouds and fog;
3. Orographic lifting, which produces clouds in the vicinity of land and sea features conducive to forced ascent and subsequent cooling of the air to condensation.

The following characteristic cloudiness features are found in several different regions of the Arctic. On account of the warm waters of the North Atlantic Drift current , wintertime cloudness in this district is by and large of the convective type. Cold outbreaks from the north in winter, when achieving the warm waters off the Norwegian current, result in a destabilization of the air with the end goal that cumulonimbus clouds are conceivable. In spite of this, cumulus clouds is less unavoidable than stratified clouds of summer and, along these lines,

winter is less overcast than summer. Overcast cover in this period achieves just up to 40 percent, while in summer it can achieve 80 percent. Since less cyclonic action happens in summer, the clouds have a tendency to be middle clouds.

In winter the central part of Russia can be expected to be dominated by anticyclonic conditions. Because of the moisture supply, however, the clearest areas are east of 100 °E at around 140 'E. The cloud type is generally cirrus about 40 percent of the time. Middle clouds occur only with rare cyclonic activity, and stratocumulus under inversions occurs only infrequently. As in the Norwegian Sea area, cloudiness is greatest over the eastern Siberian area in summer. At this time anticyclonic conditions are less frequent, and open seas are a supply of abundant moisture. This situation tends to produce low and middle convective cloudiness at this time. Spring and fall are not similar in terms of cloudiness because of the rapid freezeup in the fall that ties up the moisture supply. The gradual thaw of spring assures longer lasting or persistent cloudiness.

Because of the extensive ice cover in winter, cloudiness over the Arctic Ocean is least in winter and greatest in summer here also. In summer a high frequency of stratus and stratocumulus occurs. It may reach 80 percent during this season, as relatively warm air condenses by cooling due to the ice cover of the ocean below. These stratus clouds often exceed 1,500 ft (457 m) in thickness. The water content of these clouds diminishes from the coast to the pole, naturally. The seasonal change in cloudiness is quite rapid during the short transition periods of spring and fall [2].

1.4 Causative factors for marine fog

Advection fog—warmer airflowing over a colder sea (cold sea fog or cold fog) The sea fog investigated byTaylor (1917) has come to be labeled as advection fog —a fog that is generated through the action of air movement over a surface with a different temperature. In Taylor's study, the warm/moist air initially over the Gulf Stream was transported northward and encountered progressively colder sea surface temperatures on its path to Newfoundland. This we label cold sea fog in contrast to the opposite case where cold air is transported over progressively warmer water—the situation studied by Petterssen off the coast of southern California and labeled warm sea fog.

Focusing on the high-frequency fog area over the northwestern Atlantic, we note sea surface temperatures (SSTs) as low as 10 °C north of Newfoundland. In the other cardinal compass directions relative to Newfoundland, the SSTs are significantly warmer (the American continent to the west and the Gulf Stream to the south and east). An airflow originating from any of these warmer areas can potentially induce cooling of the near-surface marine air and eventually produce fog (Fig. 6). Taylor concluded that all fluid states (moisture–temperature structure) in these cases must map onto a straight line in the q–Θplane (q—total water mixing ratio; Θ—potential temperature) which passes through the surface state (q_0,th0) and has a slope determined by the ratio of the air–sea moisture and heat fluxes. If the turbulence effects are dominant and radiation effects are negligible, Oliver et al. (1978)showed that this condition implies that temperature and moisture fluxes are the same and that the distributions of q–q_0 andΘ–$\Theta_0$and their turbulence correlations must be functions of $z/L_m$and z/z_0,where $L_m$is the Monin–Obukhov length, z is the height, and $z_0$is the roughness length. To achieve this state, Taylor concluded that one of the most important factors was adaptation and modification of an air mass along the long overwater trajectory originating over the warm sea

surface and continuing over the cold ocean current. This use of the similarity theory complements Taylor's analysis.

1.5 Fog during coastally-trapped disturbances

Interestingly, some authors have proposed physical mechanisms different from the classical mechanisms for cold sea fog mentioned above. One example is related to fog over the cold upwelled West Coast water that appears during occasional coastally-trapped disturbances. The CTD events usually occur several times each year over the West Coast during the warm season synoptic setup (anticyclone in the northern Pacific and low over the U.S. southwest). In these areas, persistent northerly and northwesterly flow regimes are interrupted by a period of opposing southerly flow near the coast where clouds and fog are spread over several hundred kilometers of the coast and rapidly propagate northward. These conditions appear to represent a characteristic case of warm and moist air propagating northward over cold upwelled water. The main driver for the fog maintenance during the northward propagation was due to wind convergence and associated rising motions at the leading edge of the cloud/fog. The convergence and rising motions change the stability of the marine layer from strongly stable to a shallow and cool mixed layer with relative humidity increasing upward. Future studies including observations and advanced modeling are needed to further investigate these hypotheses based on testing particular model sensitivity to some of the processes such as surface fluxes.

1.6 Air mass transformation leading to fog—processes at an elevated level

The earlier discussion of sea fog clearly indicates that much of the attention has focused on the relationship between the surface atmospheric layer and the ocean surface. However, there are certainly other pathways that can bring the surface layer to near saturation over the sea. Some of the other possibilities occur in response to elevated processes above the surface layer. These include convergence and divergence above the surface layer that can change the subsidence and inversion dynamics on the top of the surface layer. Above this surface layer, the presence of clouds, haze, and particulate matter alter the upward and downward radiation. Precipitation can also affect surface layer processes. Slight changes in these factors can tip the balance for fog formation. However, a near- saturation condition can also persist without fog formation where the sum of elevated processes is a significant factor. Once formed, there are tremendous differences between cloudy and cloud-free marine layers with respect to thermal, radiative, and turbulence processes that favor maintenance of a cloudy layer [3].

1.7 Inversion and cloud forcing

Koračin et al. (2001) studied a sea fog over the West Coast of Alaska in the presence of an along-coast northerly and northwesterly flow. They emphasized a need to consider the sea fog formation and evolution in a Lagrangian framework that allows for understanding air mass modification along a long over-water trajectory. In essence, these researchers followed Taylor's lead on considering air mass transformation in a Lagrangian framework. The modification was characterized by the sea being warmer than the air with continuous cooling of the marine air along the trajectory. According to their analysis of observations and a high resolution 1D model, they concluded that the main mechanism for fog

formation was cloud-top cooling and associated turbulent mixing, supplying moisture due to apositive heat flux, and all in the presence of intense subsidence, maintained strong marine inversion, and shrinking of the marine layer along the advection trajectory.

The downward propagation of cloud cooling can be seen clearly in this time–height cross section of air temperature. The onset of cooling first occurs at higher elevations and gradually descends to lower levels. For example, the net cooling begins after 12 h of simulation at 200 m, while it takes 2 more hours for the cooling to reach the 100-m level. Significant cooling occurred after 39 h when the elevated air driven by cloud-top cooling merged with the near-surface layer. Cloud-top cooling and subsidence appear to be dominant factors for fog formation and evolution during cloud lowering along the advection trajectory. Their sensitivity tests showed that there is an optimum strength of the inversion and that moisture above the inversion controls the longwave cooling and entrainment processes.

A triggering mechanism for saturation within the shallow marine layer is still under investigation and debate. Differential advection is present—warm air advection above the inversion and cold air below the inversion. Their hypothesis is that the increased longwave flux divergence at the top of a shallow marine layer with sufficiently uniform moisture leads to condensation at the top of this shallow layer, which then rapidly propagates to the surface due to further increases in longwave cooling at the fog top. Their simulations show that longwave cooling at the interface of the warm, dry air and the moist, cool air at the very top of the depressed marine layer is the dominant process for fog formation. Sufficient mechanical and radiatively-driven turbulence initiate saturation at the very top of the marine layer, which rapidly propagates downward to the sea surface within a very shallow marine layer. Consequently, longwave cooling at the fog top is the main driver of the fog growth that is limited by the strength of the subsidence and gradual warming and drying while growing and mixing vertically.

Their sensitivity study (Fig. 4, 5) clearly indicates that the model setup (vertical resolution and physics options), and initial conditions (lower boundary—SST, humidity and temperature profiles within the marine layer, and properties above the inversion such as humidity, temperature, and subsidence) significantly influence fog initiation and evolution [3,4].
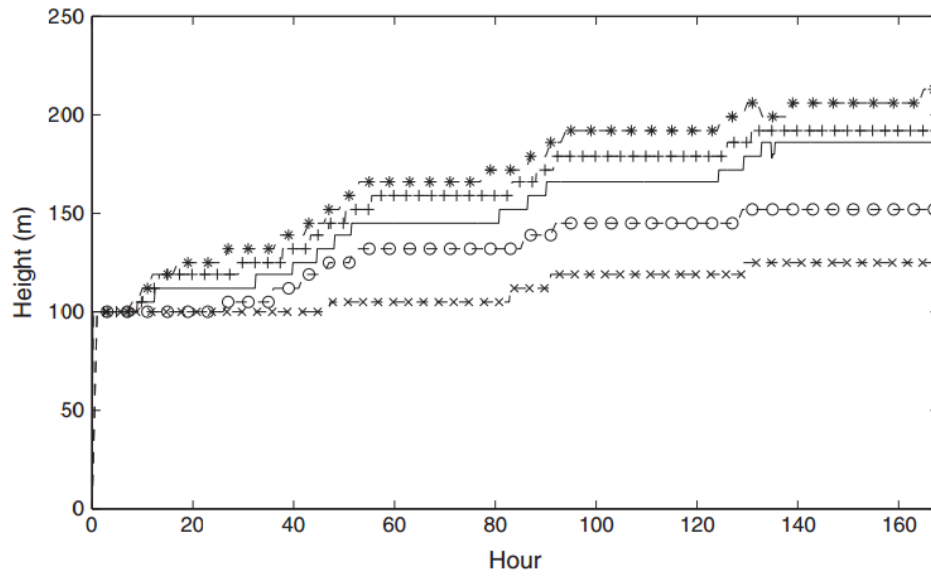

Figure 4. Evolution of the simulated fog top the baseline run (solid line). A case with colder sea-surface temperature by 2°C(○), a case with warmer sea-surface temperature by 2°C as compared to the baseline run (*), a case with larger near-surface inversion (x), and a case with drier warm-air layer (+) [7].
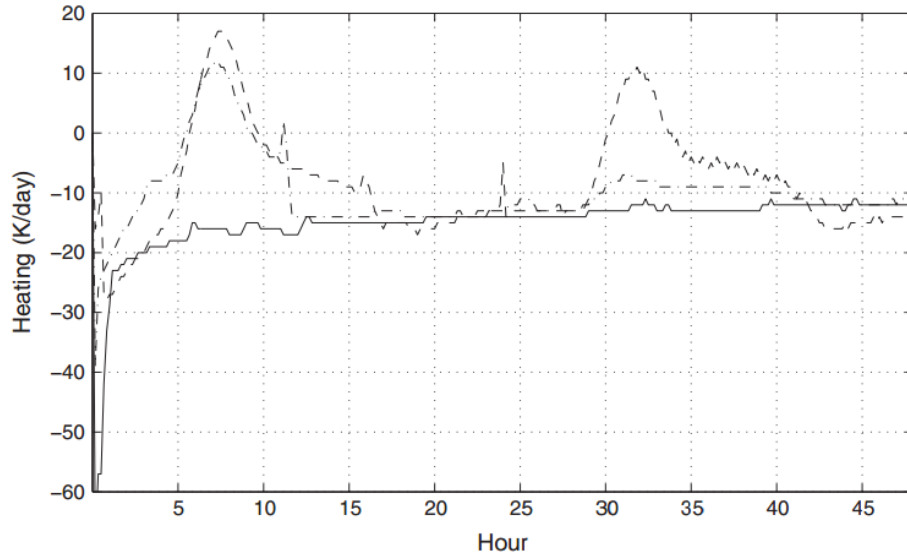
Figure.5. Time series of the stimulated average net heating of the fog layer (°C day^{-1}) due to longwave and shortwave radiative heat transfer for the baseline simulation with 180 vertical points (solid), the run with 90 vertical points (dash-dot), and the test run with 45 vertical points (dashed line) within 1200m [7].

1.8 Local circulations and advection of aerosols

While categorizing fog by advection properties, an important component is advection of aerosols and fog condensation nuclei that bears importance for fog both over the sea and land. The advection can be due to local circulations or synoptic patterns. Transport of sea aerosols and water vapor onto the land during sea breeze circulations can trigger fog over the land where the condensation nuclei came from the sea. Obviously, fog can form over the land and then drift to the sea during a land breeze and vice versa during a sea breeze. This further complicates investigation of the origin of fog and physical processes relevant to fog formation.

1.9   Fog and precipitation

Some of the early studies indicated that cloud precipitation cools and moistens the subcloud layer and lowers the condensation level. It should be noted that in many cases, this process is inaccurately called "cloud lowering".The term"cloud lowering" should be reserved for the whole entity of cloud lowering (including the cloud top).

The effect of precipitation evaporating and moistening the subcloud layer can occur for a wide range of precipitation intensities and can strongly influence fog formation, evolution and dissipation. Although the majority of the cases fall into categories of light precipitation, rain showers and snow as pre-condition forcing can also lead to fog formation. They claim that the moistening is a more dominant process compared to evaporative cooling leading to fog formation.

The Lagrangian-frame simulation of a microphysical column model shows that evaporation from raindrops departing from equilibrium, i. e., the latent heat loss from droplet evaporation does not balance sensible heat flux from the ambient air, facilitates fog formation. Consequently, they indicate that the non-equilibrium state of the falling raindrops needs to be taken into account while considering precipitation fog events [5].

1.10 Environmental impact on terrestrial systems

Advecting marine fog transports water and materials onto adjacent coastal and terrestrial systems, profoundly altering the environmental conditions of these systems. The transport of fog water droplets and their associated soluble ions, dust particles, microorganisms, and mixtures of organic and inorganic reaction products changes the hydrologic, thermodynamic, nutrient, and toxicological regimes of ecosystems along the coast. Although the interactions are variable and complex,

several prominent ecological mechanisms associated with each type of flux (water, energy, and microscopic particulates both inorganic and organic) have been elucidated. The strong ecological response to the spatial and temporal variability of marine fog results in discernible impacts on diurnal to seasonal, interannual to decadal, and longer scales.

The strong biogeographic climate signature of transported marine fog water and minerals hasled to terrestrial proxies for paleoclimate change in coastal upwelling. Expansion and contraction of fog associated vegetation is interpreted as a synchronous response to marine fog-conducive upwelling conditions that are an expression of ENSO/PDO variations. In the context of longer paleoecological timescales, fog imbued coastal regions now act as refugia for forest ecosystems that were once distributed across North America but do not tolerate current combinations of arid and freezing conditions such as redwood forests that are now restricted to a narrow 50 km belt along the California coast.

1.11 Impact on aviation

Dramatic expansion of operational weather surface observations so important for the understanding of fog and short-term forecasts occurred with the initial development of commercial. Interest in marine fog forecasting tended to be restricted to coastal airports subject to fog that included bays. In these early days, there were a disproportionate number of floatplane operations due to the major travel junctions at coastal bays and the limited number and quality of land runways. The forecasting technique tended to be based on a combination of climatology, fog-prediction diagrams and a subjective estimate of the synoptic weather trend. The latter for some stations was a subjective analysis from a central agency relying on experience, climatology, surface weather observations and soundings, performed by skilled forecasters such as C.K.M. Douglas and H.H.

Lamb in Great Britain (Lewis et al., 2004) and the National Weather Service in the U.S. Some forecasters maintained a reputation of superiority over machines in forecasting fog long into the era of central, computer-based forecasts, due to the difficulty of such systems in accurately expressing the subsynoptic scale, never mind the microscale, in the early stages of their development. More systematic collection of surface observations and balloon soundings at fixed sea locations began with the development of Ocean Weather Ships (in part the response to a Pan-American aircraft accident over the Pacific Ocean in 1938) and the heightened trans-North Atlantic ship and air traffic with the escalation of WWII. A dozen Ocean Weather Ship stations were in the north Atlantic and three were in the north Pacific starting about 1940 and ending in the 1970s.

A ten year study of aviation accidents by the US National Transportation Safety Board (NTSB) indicated that low ceiling and visibility contributed to over 20% of the accidents. Of those accidents, 68% were specifically due to fog and low ceilings (NTSB Weather Related Accidents).

Fog or reduced ceilings often cause delays, diversions, or cancellations. Nearly 74% of all delays at airports are caused by weather, with the majority of such delays caused by low ceilings and visibility. A 1996 study conducted by Massachusetts Institute of Technology (MIT)/Lincoln Labs on marine stratus at San Francisco International Airport (SFO) found that the airline and passenger cost of delays due to ceiling and visibility approached $100 million dollars per year.

Every airline has its own operations center in which they monitor their flights. Airline operations function similar to air traffic managers (see below) but their focus is on their airline. Thus, they make extensive use of aviation forecast and other weather products from multiple sources.

Airline dispatchers are a part of the operations center. They plan the fuel loads and determine flight routes based on individual aircraft capabilities,

international and national regulations, and weather, both enroute and at the destination.

National air traffic services may require a designated alternate destination on the dispatch release if either the destination airport's observed or the forecasted ceiling and visibility are less than 600 meters (2000 ft) and/or 4800 m (3 mi) within one hour either side of expected arrival time. Once it is determined that an alternate is necessary, the dispatcher must select an airport that meets the alternate minima. These minima are usually 120 m (400 ft) and 1600 m (1 mi) or 180 m (600 ft) and 3200 m (2 m). Smaller airports may require more stringent minima of 240 m (800 ft) and 3200 m (2 mi) or even 300 m (1000 ft) and 4800 m (3 mi).

If an alternate is required, regulations specify that additional fuel be carried to fly to and attempt to land at the destination airport and then fly to and land at the most distant alternate airport.

Upon arrival at either airport, there must be at least 45 minutes of fuel reserve remaining. If adverse weather conditions are occurring or forecast to occur, the dispatcher will first calculate a normal total fuel load and then add about 15% more fuel. The requirement of alternates and the costs involved in carrying additional fuel could result in millions of dollars per day for all affected flights, not including the untold hours of passenger inconvenience.

Consider this sobering statistic: Of those General Aviation (GA) pilots involved in low ceiling or low visibility accidents due to fog, more than half were fatal. Clearly, this is a user community that needs the best forecast possible.

General Aviation describes a broad spectrum of operations. For our purposes we will define GA as "other than air carrier, air taxi, or military". Most of the flying within this GA category is not-for-hire and conducted in single- and two-engine aircraft. GA pilots obtain weather briefings through government-sponsored programs or commercial vendors of weather products. Experience levels vary from

the novice private pilot to veteran airline transport pilots, and they make weather decisions based on their individual training and experience. About half of all GA pilots can only fly VFR. Consequently, clouds can be a significant hazard for this group, as well as for a number of IFR-rated pilots who have limited flying experience in these conditions [6].

Chapter 2. Operating principle of the fog and low stratus remote sensing

2.1 Visibility of fog

The vis/fog satellite images are generated from visible geostationary satellite images during local daylight hours, and from a derived "fog" image at night that emphasizes the low. During the day the visible image is brightness normalized by dividing by the cosine of the solar zenith angle. This removes most of the image dependence on sun angle, such as brightness changes at sunrise and sun set and differences between winter and summer image brightness. The visible brightness depends primarily on the thickness of the cloud. The visible image is used when the sun is higher than 3 degrees above the horizon.

Fog and Stratus are found in satellite pictures as low-level cloud sheets with a variable even degree. Little nearby fixes of haze are hard to recognize in satellite images (estimate in the request of a couple of kilometers). Nonetheless, expansive zones of mist and stratus can cover regions more than hundreds or thousands of square kilometers, and they are effectively seen in Meteosat Second Generation. Particular example highlights identified with various St/fog sorts:

•The edges of radiation St/fog over land sharp however sporadic, every now and again limited by territory highlights.

•Over the seas the edges are smoother.

•Valley fog is anything but difficult to recognize, since its dendritic edges take after the stature shapes of the valleys.

•Advection St/fog has a more customary edge design than radiation haze, which is confined by the landscape highlights.

Visibility	Description	Visibility	Description
Less than 40 meters	Dense Fog	2-4 km	Haze
40-200 meter	Thick Fog	4-10 km	Poor Visibility
200-1000 meter	Fog	10-40 km	Good Visibility
1-2 Km	Mist	More than 10 Km	Excellent Visibility

Table 1. Visibility conditions and description [15].

At night there are no visible images, so a derived "fog" image is substituted for the visible. The "fog" image is generated from the temperature difference between the 3.7 micron images and the 11 micron infrared images. The temperature difference depends primarily on emissivity differences caused by different physical characteristics of the radiating surfaces. The brightness of the image is set up so that low clouds are white, ground is gray, high clouds are black, and very high cold thunderstorm tops are a salt and pepper black and white.

The "fog" image is not very sensitive to the temperature of the low clouds except for extremely cold surface temperatures below -40 degrees, when it starts to show some of the salt and pepper appearance. The ground generally shows up as a gray color, except for a few areas in the west, such as the delta of the Colorado River which shows up white because of the soil emissivity there. The white "fog" low clouds start to show up on the images when the low clouds are wider than 2 miles, and are thicker than about a hundred feet. Hence it will generally pick up widespread IFR condition, but may not show small, thin local fog or haze conditions.

Satellite imagery is used to identify low clouds and fog both in conjunction with in-situ field studies and operationally by meteorological service. The standard

approach to detecting fog relies on detection of passive infrared emission or scattering from the cloud-top. This is achieved by evaluating the difference between the narrow-band brightness temperature observed in the infrared window region of the spectrum (typically a wavelength in the 10–12 μm range) and a brightness temperature observed in the near-infrared (typically in the 3–4μmrange).The emissivity of both increases with cloud depth, but the difference is relatively uniform for clouds thicker than approximately 100 m.

For low, liquid water clouds, the infrared window channel emissivity is greater than the near-infrared emissivity, leading to a positive difference (window channel minus near-infrared channel) in the observed brightness temperatures that increases with cloud thickness. At night, the difference is small (generally less than2 °C) for clear-sky conditions and increases to as much as approximately 5 °C for thick stratus or stratocumulus clouds. Thin cirrus clouds yield a negative brightness temperature difference that distinguishes them from lower liquid water stratus clouds. Fig. 19 shows an operational application of the technique applied to GOES 15 geostationary satellite imagery depicting nighttime low clouds and fog intruding on the San Francisco Bay Area. In addition to the presence of fog, depth of the fog based upon the brightness temperature difference is also estimated operationally.

During the day, the signal of reflected near-infrared radiation from the sun overwhelms the emission signal. However, the near-infrared reflectance of low liquid water cloud is substantially brighter than the reflectance of surface or cirrus clouds, which generally yields a large negative brightness temperature difference useful for daytime detection of fog and low stratus clouds (Fig. 6) . The infrared brightness temperature difference technique is applicable over the ocean and a wide variety of land surface types. It has been applied in a range of fog studies [7].
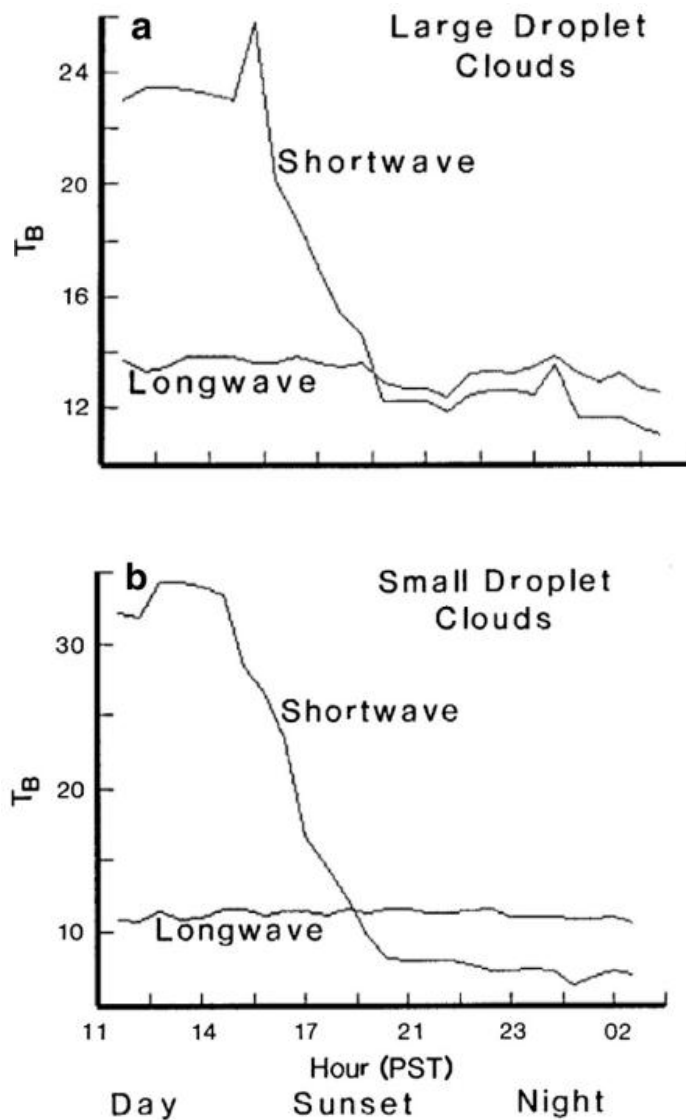
Figure.6. Infrared window channel brightness temperature (longwave) and near-infrared channel brightness temperature (shortwave) illustrating the change in sign of the brightness temperature difference at sunset [9].

One fundamental limitation of this approach is that it does not precisely discriminate cloud near the surface from higher level stratocumulus or altostratus clouds. Higher-level clouds may either obscure fog below or be mistaken for low-level clouds. Furthermore, even for low clouds, the infrared mission signatures of the cloud measured from above yield little information regarding the proximity of the cloud base to the surface. One solution to this problem is combining satellite data with information about surface conditions. The successful fog detection rates using satellite imagery compared against surface monitoring stations in Canada

are only between 0.26 and 0.32, largely owing to the presence of mid- or high-level clouds. However, they improve the rate to between 0.55 and 1.00 by using numerical weather prediction model-derived near-surface temperature estimates. They report a false alarm rate of only 0.10.

Daytime application of the brightness temperature difference technique is also complicated by large variations in near-infrared illumination from the sun through the day. Some documents show the large daytime variation in the brightness temperature difference through the day, and demonstrate that the daytime detection of fog and low cloud is made more reliable by first estimating the near-infrared reflectance, which is a considerably more stable quantity through the day, and using the high reflectance of low stratus clouds to distinguish fog and low cloud from less reflective cirrus, ocean, or land surface. Nevertheless, further ambiguity in the brightness temperature difference is present in the dawn and dusk hours, when the weak signal in reflected near-infrared radiation renders fog indistinguishable from the surface in the brightness temperature difference. Lee et al. (2011)make use of the cloud-free visible reflectance derived from 15 days of prior satellite imagery to identify scenes that are brighter than the cloud-free case and distinguish brighter fog in the visible band from darker surface.

Based on the daytime and nighttime brightness temperature difference and the additional dawn/dusk criterion, Lee et al. (2011)presents a smooth 24-hour fog detection algorithm. The limited visibility caused by fog is a consequence of the microphysical aspects of the cloud. Detection of the potential presence of fog using satellites is valuable, but further interpretation of the potential impact on visibility relies on retrieval of the microphysical properties of the clouds. The reflectance of near-infrared radiation, which has so far been discussed as a means of detecting daytime fog, is also substantially dependent upon the size of the cloud droplets. A cloud composed of smaller drops enhances the reflectance of near-infrared radiation relative to a cloud with larger drops. Near-infrared reflectance, when combined with a measure of visible reflectance (for example at 0.64μm), has been

used to perform a combined retrieval of cloud optical thickness and cloud droplet effective radius.

These data are now produced routinely using imager data such as that from the MODIS instrument. The potential to estimate the surface visual range in the presence of fog based on some assumptions about the vertical profile of the drop sizes. Retrievals of cloud drop number concentration are also made by satellite with some success, which could be applied to translating satellite observations to surface visibility estimates. This retrieval, however, also relies on an assumption for the vertical structure—in this case the adiabatic model for the vertical variability of LWC and drop effective radius.

Active remote sensing of fog can eliminate some of the ambiguity of satellite remote sensing, but at present is limited to select surface sites, and hence does not offer the global coverage of satellite data. Visible light is strongly attenuated by clouds, therefore lidar technology deployed from the surface is useful for detecting cloud base, such as with operational ceilometers. However, such technology cannot profile a fog layer. Suborbital aircraft and satellite lidar systems can identify cloud top heights with substantially greater precision than passive infrared imaging techniques, but are similarly unable to determine whether the cloud base reaches the surface. Radar systems have been used to study the structure and evolution of fog layers. Operational weather radars operating at centimeter wavelengths are designed to detect precipitation sized cloud drops, but the smaller drops typical of fog layers do not effectively scatter radar signals at these wavelengths. Experimental cloud radars, however, have been deployed at 35 GHz and 95 GHz frequencies to study the layer thickness and vertical structure of cloud layers. Hamazu et al. (2003) describe a scanning Doppler radar system at 35 GHz and use it to describe the variability of reflectivity within a sea fog case. Gultepe et al. (2009) and Boers et al. (2013) evaluate the prospects for determining surface visibility from radar reflectivity. While relationships between the two quantities are apparent, that was conclude that the visibility–reflectivity relationship varies as the

fog layer evolves. A 94 GHz satellite cloud radar, CloudSat, is in orbit, offering the prospect of global fog studies. However, weak sensitivity and clutter attributable to the surface return complicates the observation of cloud properties near the surface by space-borne radar. Operational techniques for satellite remote sensing of sea fog based on passive visible and infrared imagery are now routinely applied to monitoring fog events. These techniques work best at night and are limited in their ability to distinguish fog at the surface from ordinary low stratus clouds. Active remote sensing of fog by radar shows potential for retrieving visibility estimates in fog layers, but is so far limited to experimental cases rather than widespread monitoring [8].

2.2. Cloud particle spectrum

The cloud particle spectrum is represented by the superposition of two lognormal size distributions with a standard deviation of 1.4: one for cloud droplets and the other for ice crystals. This choice of size spectrum is based on simulations with the GB2001 reference model and observations.

In spite of the fact that perceptions show that the gamma sizxe distribution can likewise be utilized to represent to cloud spectra in models, the lognormal appropriation is favored here since it is more illustrative of the cloud spectra gotten with the express model, which has been utilized to build up the parameterization displayed in this paper. The standard deviation of size of the cloud droplets conveyance shifts as per cloud type. In ice or low stratus, the standard deviation normally extends from 1.2 to 1.4. Above the sea surface low stratus cloud an expansion in the standard de-viation with diameter is observed.

The couple of accessible observations of diamond dust in the Arctic recommend a comparative connection between the mean width and the standard

deviation. So as to improve the parameterization, a remarkable incentive for the standard deviation of the cloud estimate dispersion has been picked.

To describe cloud liquid and ice particle size distributions, four prognostic variables are used: the mean diameter of cloud droplets (Dw), the mean diameter of ice crystals (Di), the cloud ice mixing ratio (qi), and the cloud water mixing ratio (qw).

These parameters along with the fixed standard deviation of 1.4 describe the cloud spectrum at each time step. The time evolution of these variables can be expressed as follows:

$$\frac{\partial q_w}{\partial t} = PCS + PCC + PCI - \frac{m(D_w)}{\rho \Delta t}(\Delta N_h + \Delta N_g) + K\frac{\partial^2 q_w}{\partial z^2} \tag{1}$$

$$\frac{\partial q_i}{\partial t} = PIS + PID + PII + \frac{m(D_w)}{\rho \Delta t}(\Delta N_h + \Delta N_g) + K\frac{\partial^2 q_i}{\partial z^2} \tag{2}$$

$$\frac{\partial D_w}{\partial t} = \frac{1}{\Delta t}\left[\left(\frac{-6\rho q_w}{\pi \rho_w}\right)^{1/3}\left(\frac{1}{\Delta N_h} + \frac{1}{\Delta N_g} + \frac{1}{\Delta N_{nw}} - \frac{1}{\Delta N_c}\right)^{1/3} + \left(\frac{6\Delta m_{iw}}{\pi \rho_w}\right)^{1/3}\right] + K\frac{\partial^2 D_w}{\partial z^2}$$

$$\frac{\partial D_i}{\partial t} = \frac{1}{\Delta t}\left[\left(\frac{-6\rho q_w}{\pi \rho_w}\right)^{1/3}\left(\frac{1}{\Delta N_h} + \frac{1}{\Delta N_g} - \frac{1}{\Delta N_c}\right)^{1/3} + \left(\frac{-6\rho q_i}{\pi \rho_i \Delta N_{ni}}\right)^{1/3} + \left(\frac{6\Delta m_{ii}}{\pi \rho_i}\right)^{1/3}\right] + K\frac{\partial^2 D_i}{\partial z^2} \tag{3-4}$$

where PCC, PCI, PID, PII are, respectively, the condensation/evaporation rate onto/of cloud water droplets, the deposition/sublimation rate onto/of cloud ice crystals, the nucleation of water droplets, and the nucleation of ice crystals; PCS and PIS are, respectively, the sedimentation rate of cloud water droplets and ice crystals; Nh and Ng are, respectively, the number concentration of cloud water droplets that freeze heterogeneously and homogeneously; Nc is the number of concentration of water droplets or ice crystals that collide to form larger cloud particles; Nnw and Nni are respectively, the number concentration of water droplets and ice crystals nucleated; miw and mii represent the mass of condensed/evaporated water and deposited/sublimated water, respectively; K, r,

rw, ri, and Dt, re, respectively, the eddy diffusion coefficient, air density, water density, ice crystal density, and model time step. Here D indicates the variation of the variable during a time step (Dx5xt1Dt 2xt).

To compute the microphysical processes like condensation and aerosol activation, it is necessary to know the time evolution of the saturation ratio (S). Unlike in most climate models that set a threshold for S, in this model S is free to evolve above the saturation point and depends on the total condensation/deposition rate and the atmospheric temperature cooling rate:

$$\frac{\partial S}{\partial t} = -\frac{L}{R_{\vartheta}T}\frac{\partial T}{\partial t} - \frac{p}{\varepsilon e_s}(PCC + PCI + PID + PII)$$
(5)

Where Ry, es, p, T are, respectively, the gas constant for water vapor, vapor partial pressure at water saturation, air pressure, and air temperature. Here 5Ry/Rd where Rd is the gas constant for dry air. In this expression, variations of S associated with vertical velocity is included in the cooling rate term dT/dt. The LCM – model also simulates explicitly the aerosol size distribution. The model allows for several tracers and it is assumed that aerosols are internally mixed. The eleven size bins cover aerosol sizes ranging from 0.01 to 8 mm in diameter. The following equation is used to predict the aerosol number concentration (Nkl) for each tracer l:

$$\frac{\partial N_{kl}}{\partial t} + V \cdot \nabla N_{kl} + \omega\frac{\partial N_{kl}}{\partial p} = S_{nucl} + S_{dep} + S_{wdep} + \frac{N_a}{\Delta t}$$
(6)

Where V is the horizontal component of the wind and V is the vertical component of the wind. Here Snucl , Sdep, Swdep represent the nucleation of aerosols, dry, and wet deposition. Na is the aerosol number concentration that is activated to form either water droplets or ice crystals. The advection terms on the left-hand side are given through the RIM utilizing local observations at the purpose

of intrigue. Week by week mean concentration of aerosol at the surface are accessible from the atmosphere chronicle. We accepted a consistent aerosol concentra-tion in the vertical from the surface to 5 km and amid the week. This assumption may show up in inconsistency with a few observations that demonstrate important varieties in the vertical.

However, there is no common denominator between observations with regard to the variation of aerosol concentration with height. It generally depends on the presence of clouds and on the air layer origin, which vary as a function of height. Consequently, it is a simpler and unambiguous choice to assume a uniform vertical structure in the absence of measurements. Equations (1)–(6), along with the traditional dynamical equations (continuity equation, thermodynamic equation, hydrostatic equation, and momentum equation) form the system of prognostic equations used in the LCM - model. In the next section, a description of the parameterization developed to represent the microphysical processes present in Eqs. (1)–(6) is presented [8,9].

2.3. Microphysical processes

A large portion of the microphysical processes impacting on ice crystals rely on upon its shape and density. Therefore, with a specific end goal to parameterize the physical processes including ice crystals, one needs to describe the its shape. Instead of water droplets, ice crystals have diverse shape and density depending on the temperature and supersaturation. A vast assortment of crystals propensities have beenv observed in the Arctic. Nonetheless, research facility tests and observations have demonstrated that section and needle crystals shapes appear to command at the icy temperatures and high relative humidity normal for the ice winter. Given :

1) the extraordinary multifaceted nature of building up an ice cloud parameterization accounting for a some crystals propensities

2) the exceptionally restricted information

furthermore, instability winning in this field, the issue is streamlined by accepting a solitary crystal shape. A segment needle shape is accepted in our reproduction with a length/radius proportion of 10. Albeit to some degree discretionary, this proportion concurs with a few perceptions over the Arctic zone amid winter. Likewise, this crystal shape is by all accounts dominating in low temperatures and in contaminated airmass features of the Arctic during winter.

Warm fog appears when T>0 °C and its measurements can be done fairly accurate. There is a problem that a lot of the visibility sensors are calibrated at warm temperatures and they are not tested at cold T<-20 ° C. Freezing fog appears when surface T goes below 0 °C. Its measurements can be difficult, when sensors get icing conditions although heating systems exist. Under the icing conditions, some of the visibility sensors do not response properly and this may cause problems for real time freezing fog observations. When NWP models do not have accurate predictions of T and RH, then freezing fog conditions may not be predicted accurately. Steam fog conditions occur when cold air moves over warm water surfaces and these results in steam fog and, over the Arctic regions, fog or low cloud forms over the leads and polynyas that are directly related to steam fog conditions. When freezing of the droplets formm, shattering may occur and resulting in secondary ice crystal formation over the cold climatic regions. Prediction and observations of ice fog conditions are more difficult than these of low latitudes because of unknown cold microphysical processes and instrumental issues. Therefore, NWP models need to be developed in order to account of ice nucleation processes and cold weather conditions [10].

2.4. Remote sensing retrievals of fog

Remote sensing of fog properties is difficult because of surface conditions and shallow fog layers, low density of the mass, and small size of the particles (<10-15 microns). The main remote sensing platforms for fog real-time detection and nowcasting can be listed as satellites, microwave adiometers, ceilometers and sodar, and reflectivity based radar systems, and lidars. It is tightly correlated to the temperature inversions detected on the balloon soundings and shown with up triangles (bottom of inversions) and down triangles (top of inversions). The black spots show the maximum altitude reached by the meteorological balloons. No inversion was detected on soundings with a maximum altitude below the red sodar reflectivity layer. The main concept of behind the satellite based fog forecasting of warm marine fog is that fog droplets response to 3.9 μm channel (IRSW) of the satellite bi-directional reflectance is large due to their absorption compared to ice crystals but day time effect on IRSW channel due to SW radiation becomes large that needs to be taken away from the IRSW reflectance. This may result in significant uncertainty of retrieval applications during day time retrievals.

An example of fog detected using this method is given in next section. In the case of cold fog conditions, because of snow at the surface and ice clouds in the Arctic inversion layers, this technique may also include severe issues. The distinction made by satellite data between ground fog and low stratus is also an important issue. A detection scheme developed by Bendix et al (2005) provided a discrimination method between low stratus and fog. Based on their method, stratus base height can be computed and compared with terrain height at a specific pixel that can be used for fog and low cloud determination [10].

2.5. Methods of fog detection

In order to address different spatial and temporal scales and highlight the potential of different spectral resolutions, three different systems were used: NOAA AVHRR, Terra/Aqua MODIS and Meteosat 8 SEVIRI. While the former two, as polar orbiting systems, offer better spatial resolutions, the latter system features a very good temporal resolution of 15 minutes.

The detection of the area covered by fog and low stratus (FLS) is tackled in different manners for different times and systems. This subsection will highlight the newly developed parts. For daytime MODIS data, several cases of fog of varying thickness were simulated using a radiative transfer model for all channels in the visible range. A pixel is identified as FLS-covered if its visible channel signals fall between the minimum and maximum computed for each wavelength. Figure 1 shows the areas identified in this way for a sample scene for all MODIS visible channels.

The SEVIRI instrument aboard the Meteosat Second Generation series satellites has a much smaller number of channels in the visible range. Therefore, an entirely different algorithm was devised for this instrument. As the spectral potential is more limited, spectral tests are complemented by spatial analysis of coherent pixel areas. FLS is addressed diagnostically as a low water cloud close to the ground and composed of small droplets. Each of these assumed properties is tested for with one or more tests. The testing sequence is shown in figure 7.
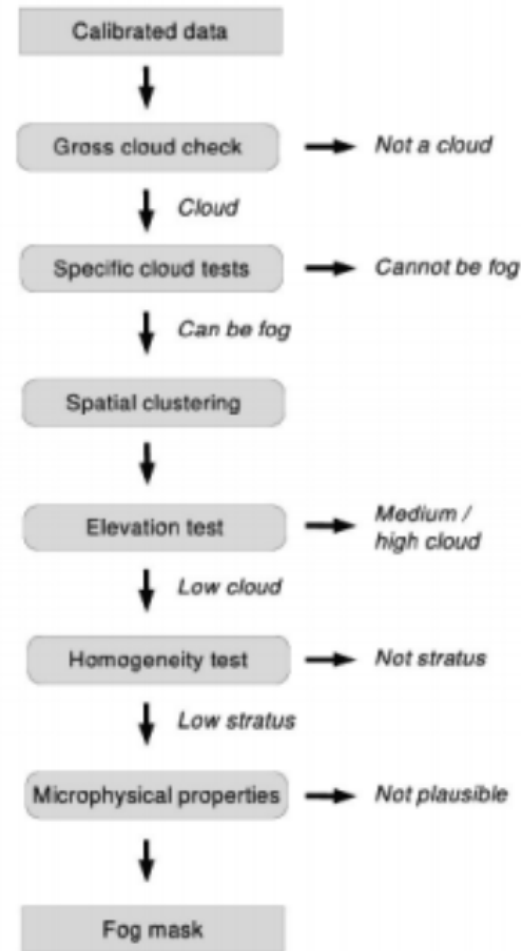
Figure 7. Testing sequence applied for FLS identification in SEVIRI data [10].

After some initial spectral tests all potentially FLS-covered pixels are clustered spatially into discrete and coherent areas of pixels. These entities are then analysed for height and surface homogeneity to determine whether they can be FLS. The spatial tests are applied without modification throughout the day. However, not all of the spectral tests are applicable at all solar elevations. At night, the initial delineation of FLS areas makes use of the emissivity differences observed for small droplets at 3.9 and 10.8μm. The technique commonly makes use of a fixed threshold of blackbody temperature difference in these two channels. However, the 3.9 μm channel on SEVIRI has an exceptional spectral width and overlaps with the CO_2 absorption band around 4.2 μm. With seasonal and regional differences in atmospheric CO_2 concentration, a technique for dynamic threshold

determination is needed. This has been developed and implemented on Meteosat SEVIRI [11].

2.6. Ground fog detection and fog properties

Once the FLS area has been identified, a decision is needed on whether or not the cloud is in contact with the ground at a given location, i.e. whether fog is encountered. This decision is reached based on a comparison of computed cloud base height (zb) with surface elevation (zs): zb = zs --> fog In order to obtain cloud base height, cloud top height and cloud thickness need to be known, because zb = zt − åz where zt is cloud top height and åz cloud geometrical thickness. Cloud top height is obtained by interpolation of cloud margin heights into the cloud area. The margin heights are extracted from limiting terrain or an atmospheric gradient, depending on the relief situation. For cloud thickness computation, two different techniques have been developed for MODIS and SEVIRI. Both techniques require cloud microphysical parameters as input. Cloud optical thickness IJ and droplet effective radius ae are retrieved based on a lookup table of cloud radiative properties at two wavelengths: one non-absorbing (0.6) and one absorbing (3.9). The signal in the former depends mostly on cloud optical thickness, while the latter is governed by droplet effective radius (see Fig. 7.1). Since the non-absorbing channel is available at daytime only, the separation of low stratus and fog can only be performed at this time as well.
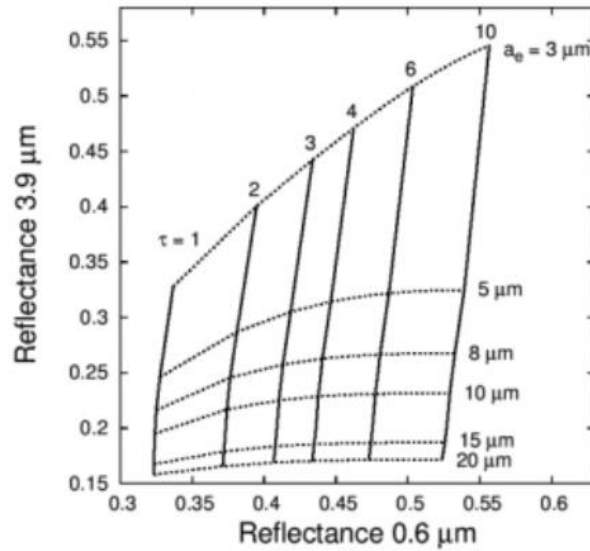
Figure 7.1. Absorbing and non-absorbing wavelength signal as a function of microphysical parameters [13].

For MODIS, a radiative transfer parameterization is used to compute cloud thickness. The radiative signal of cloud is simulated in all visible wavelength channels in dependence on cloud geometrical thickness and microphysical parameters. The underlying assumption is that wavelength-dependent photon penetration depths reveal the vertical cloud profile. The simulation results are then parameterized and used to derive cloud geometrical thickness from channel signals and microphysical parameters. For SEVIRI data, with a reduced spectral potential, a different algorithm was developed and implemented. Again, cloud microphysical parameters are computed as a precondition. Since cloud geometrical thickness cannot be derived directly, it is put in relation to cloud liquid water path (LWP), which can be computed from cloud optical thickness IJ and droplet effective radius ae as: LWP = 2/3 IJ ae The pattern of vertical cloud liquid water distribution is modelled and iteratively fitted to observed LWP, cloud top height and cloud top temperature. Once agreement is reached, cloud base height can be derived. From the distance of computed cloud base and surface elevation a fog confidence level is computed as the final product [11,12].

2.7. Product description of MODIS

The MODIS Cloud Product combines infrared and visible techniques to determine both physical and radiative cloud properties. Day by day worldwide Level 2 information are given. Cloud-molecule stage (ice versus water, fogs versus snow), powerful cloud-molecule range, and cloud optical thickness are inferred utilizing the MODIS visible and close infrared bands radiances. A sign of cloud shadows influencing the scene is additionally given. Cloud-top temperature, height, effective emissivity, phase (ice vs. water, opaque vs. non-opaque), and cloud division are delivered by the infrared recovery techniques both day and night at 5x5 1-km-pixel resolution. At long last, the MODIS Cloud Product incorporates the cirrus reflectance in the obvious at the 1-km-pixel resolution, which is valuable for expelling cirrus scattering impacts from the land-surface reflectance product. There are two MODIS Cloud data product files: MOD06_L2, containing information gathered from the Terra platform; and MYD06_L2, containing information gathered from the Aqua platform.

An intensive portrayal of worldwide darkness and its related properties is basic to the MODIS mission for two reasons. In the first place, fogs assume a basic part in the radiative adjust of the Earth and should be must be accurately described in order to assess atmosphere and potential environmental change precisely. What's more, the presence or absence of cloudiness must be precisely decided so as to recover legitimately numerous environmental and surface parameters. For a significant number of these recoveries, overcast cover, even thin cirrus, speaks to pollution. Key radiative properties of fogs, for example, phase, optical thickness, and temperature might be recovered utilizing MODIS instruments with phenomenal determination.

2.7.1. Additional Information

- Coverage: Global

- Spatial/Temporal Characteristics: Resolutions of 1 km or 5 km/once or twice per day (varies with parameter)

- Key Science Applications: Cloud parameterization, climate modeling, climate monitoring, increasing accuracy of other MODIS retrievals

- Key Geophysical Parameters: Cloud-particle phase (two algorithms), cloud-particle size and optical thickness, cirrus reflectance at 1.375 μm, and cloud-top temperature, emissivity, and height

- Processing Level: 2

- Product Type: Standard, at-launch

- Maximum File Size: 65 MB

- File Frequency: 288/day

- Primary Data Format: HDF-EOS

2.8. Data Set Evolution

The determination of cloud-top properties will require the use of MODIS bands 29 and 31-36, along with the cloud-mask product (MOD35), to screen for clouds. In addition, NCEP or DAO global model analyses of surface temperature and pressure, profiles of temperature and moisture, and blended SST analyses will be required in the calculation of cloud forcing as a function of atmospheric pressure and emissivity. The Menzel cloud-phase algorithm will require MODIS bands 29, 31, and 32 and analyses of surface emissivity.

The validation of cloud-top heights will be conducted through comparisons with stereo determinations of cloud heights from GOES and lidar estimates and aircraft observations of cirrus heights. Cloud emissivity will be compared to lidar-determined values. These interim products will be used in concert with field campaigns with the MAS instrument. The Menzel cloud-phase parameter will be validated using HIRS/AVHRR data and by comparison to the King cloud-phase parameter.

The King cloud-phase algorithm requires product MOD 02, calibrated multispectral radiances. Cloud-particle size and optical thickness require these radiances plus the cloud-top parameters within MOD06 and the Menzel cloud-phase parameter. In addition, these parameters require MODIS product MOD43 (surface reflectance) and the NCEP or DAO analyses and profiles described above. The validation and quality control of these products will be performed primarily through the use of in situ measurements obtained during field campaigns and with the use of the MAS instrument.

2.9. TERRA (Moderate Resolution Imaging Spectroradiometer)

MODIS observes the ocean, atmosphere, land, and ice. With its sweeping 2,330-km-wide viewing swath, MODIS sees every point on our world every 1-2 days in 36 discrete spectral bands. Consequently, MODIS tracks a wider array of the earth's vital signs than any other Terra sensor. For instance, the sensor measures the percent of the planet's surface that is covered by clouds almost every day. This wide spatial coverage enables MODIS, together with MISR and CERES, to help scientists determine the impact of clouds and aerosols on the Earth's energy budget.

In addition to recording the frequency and distribution of cloud cover, MODIS measures the properties of clouds such as the distribution and size of cloud droplets in both liquid water and ice clouds. MODIS also measures the properties of aerosols—tiny liquid or solid particles in the atmosphere. Aerosols enter the atmosphere from manmade sources like pollution and biomass burning and natural sources like dust storms, volcanic eruptions, and forest fires. MODIS helps scientists determine the amount of water vapor in a column of the atmosphere and the vertical distribution of temperature and water vapor—measurements crucial to understanding Earth's climate system.

MODIS is ideal for monitoring large-scale changes in the biosphere that are yielding new insights into the workings of the global carbon cycle. MODIS measures the photosynthetic activity of land and marine plants (phytoplankton) to yield better estimates of how much of the greenhouse gas is being absorbed and used in plant productivity. Coupled with the sensor's surface temperature measurements, MODIS' measurements of the biosphere are helping scientists track the sources and sinks of carbon dioxide in response to climate changes.

Almost every day over the entire globe, the sensor monitors changes on the land surface, thereby building upon and extending the heritage begun by Landsat. MODIS maps the areal extent of snow and ice brought by winter storms and frigid temperatures. The sensor observes the "green wave" that sweeps across continents as winter gives way to spring and vegetation blooms in response. It sees where and when disasters strike—such as volcanic eruptions, floods, severe storms, droughts, and wildfires—and will hopefully help people get out of harm's way. MODIS' bands are particularly sensitive to fires; they can distinguish flaming from smoldering burns and provide better estimates of the amounts of aerosols and gases fires release into the atmosphere.

MODIS sees changes in the Pacific phytoplankton populations that may signal the onset of the famous El Niño/La Niña climatic siblings well ahead of their arrival. In turn, by coupling its sea surface temperature and ocean color

measurements, MODIS has observed the impacts El Niño and La Niña have on the microscopic marine plant. MODIS also has a unique channel for measuring chlorophyll fluorescence. All plants bombarded with light begin to glow, or fluoresce, but in wavelengths that our eyes cannot see. The more plants fluoresce, the less energy they are using for photosynthesis. Thus, MODIS not only maps the distribution of phytoplankton, it also helps us gauge its health.

Another MODIS instrument flies aboard Terra's sister ship—Aqua [13, 14].

2.10. Bands characteristics

MODIS is a 36-band scanning spectroradiometer (see Appendix A). Four of these visible (0.645 µm) and near-infrared (1.64, 2.13, and 3.75 µm) spectral bands will be used in our daytime shortwave cloud retrieval algorithm over land surfaces, with 0.858 or 1.240 µm replacing 0.645 µm over ocean and bright snow/sea ice surfaces, respectively. Other bands in the thermal region, such as the 8.55, 11.03, 12.02, 13.335, 13.635, 13.935 and 14.235 µm bands, will be used for cloud cover and cloud top properties (including cloud top altitude, cloud top temperature and thermodynamic phase.

In addition, the 11.03 µm band will be used to make the thermal emission correction to the 3.75 µm band during the day. Figure 8 shows the wavelength locations of these primary MODIS shortwave bands, located in the water vapor window regions.

The characteristics of band center and band-width, as well as the dynamic range and main purpose(s) of each band, are also summarized in Table 2 (see Appendix A). The 0.645, 2.13 and 3.75 µm bands will be used to retrieve the cloud optical thickness and effective particle radius over land (with 0.645 µm replaced by 0.858 µm over oceans and 1.24 µm over snow and sea ice surfaces); a

combination of the 0.645, 1.64, and possibly the 2.13 μm bands will be used for cloud thermodynamic phase determination [14].
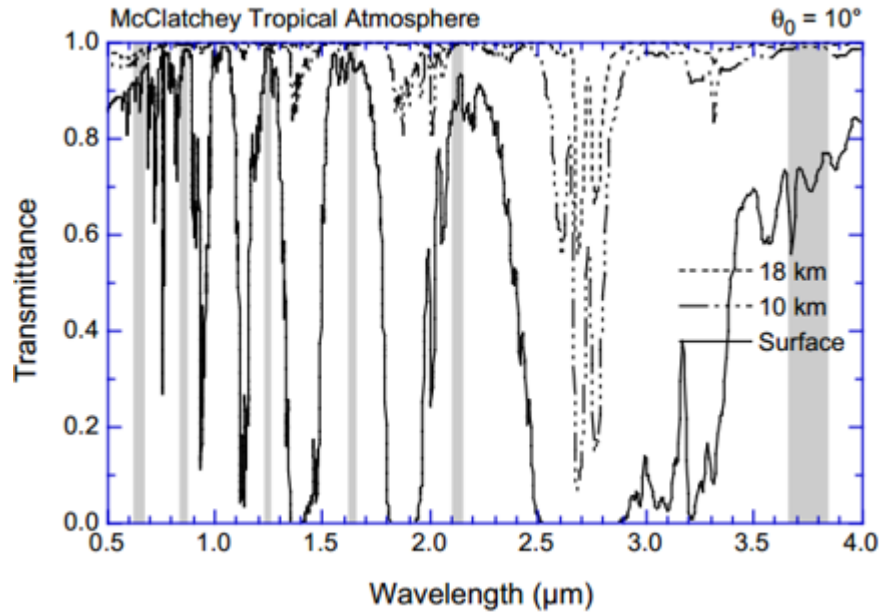
Figure 8. Spectral characteristics of six MODIS bands, centered at 0.65, 0.86, 1.24, 1.64, 2.13, 3.75 μm, used for cloud property detection. The transmittances of the atmosphere are calculated at 18 km, 10 km and at the surface at 10° solar zenith angle [14].

MODIS is designed to scan through nadir in a plane perpendicular to the velocity vector of the spacecraft, with the maximum scan extending up to 55° on either side of nadir (110° aperture). At a nominal orbital altitude for the E S AM-1 spacecraft of 705 km, this yields a swath width of 2330 km centered on the satellite ground track. In the baseline concept, the Earth-emitted and reflected solar radiation is incident on a two-sided scan mirror that continually rotates about an axis aligned with the direction of flight.

Following the scan mirror is a telescope and a sequence of three dichroic beam splitters that further subdivide the incoming radiation into four focal planes. The 3.75 μm band uses a tenelement linear array detector for the 1000 m spatial resolution bands, a 20-element array for the 500 m bands at the 1.64 and 2.13 μm

bands, and a 40-element array for the 250 m band at 0.645 µm. They are aligned parallel to one another such that a single scan of the scan mirror is imaged on the focal plane for a swath 10 km in the along-track direction and 2330 km in the cross-track direction. In this configuration, all bands within a single focal plane are simultaneously sampled and registered within 0.1 pixel, with registration errors of less than 0.2 pixels between focal planes. The signal-to-noise ratio ranges between 57 and 1100 at a solar zenith angle $\theta 0 = 70°$, depending on band, and is considerably larger than these values at the solar zenith angle and scene temperature typical of the EOS AM-1 orbit ($\theta 0 = 22.5°$).

Figure 9 illustrates the spherical albedo as a function of wavelength for water clouds containing various values of the effective radius.
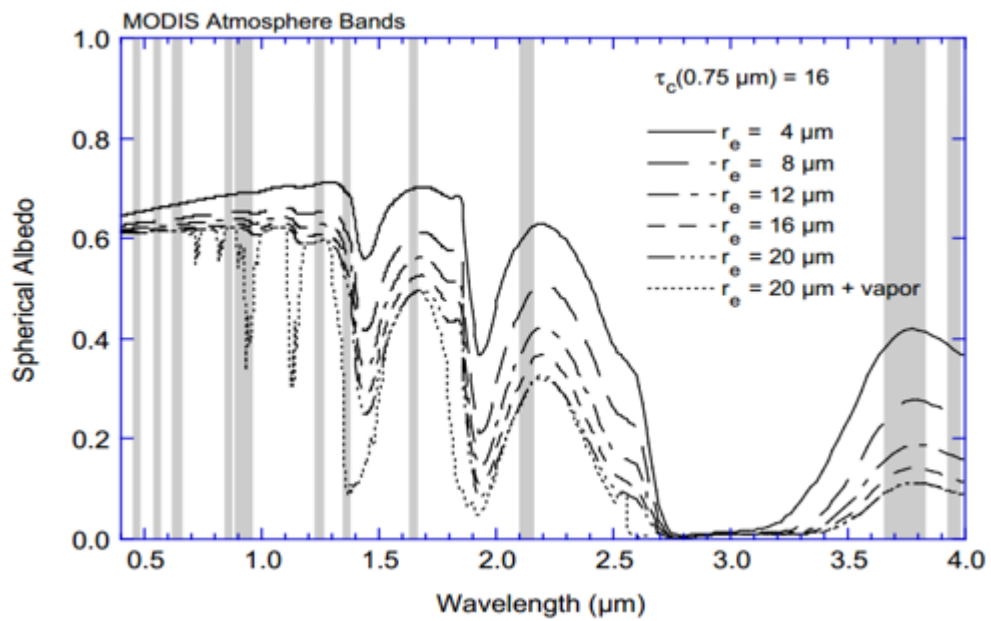
Figure 9. Cloud spherical albedo as a function of wavelength for selected values of the effective radius of cloud droplets [14].

The spherical albedo represents a mean value of the reflection function over all solar and observational zenith and azimuth angles, the reflection function itself must have a similar sensitivity to particle size. These computations were performed using asymptotic theory for thick layers and the complex refractive indices of liquid water.

These computations strictly apply to the case when τc (0.75 μm) = 16 and Ag = 0.0, and properly allow for the optical thickness and asymmetry factor to vary with wavelength in accord with our expectations for clouds composed solely of liquid water and water vapor. Since the similarity parameter is nearly zero (conservative scattering) in the water vapor windows at wavelengths $\lambda < \sim 1.0$ μm, the cloud optical thickness can be derived primarily from reflection function measurements in this wavelength region.

Figure 9 also shows that the spherical albedo, and hence reflection function, is sensitive to particle size at wavelengths near 1.64, 2.13, and 3.75 μm, wavelengths for which water vapor absorption is small. Cloud properties can also be estimated from the thermal bands.

Figure 10 shows the top-of-the-atmosphere brightness temperature as a function of wavenumber (wavelength) from 600-3340 cm-1 (3-16.7 μm) for both clear and cloud sky conditions, where all computations were made using the discrete ordinates radiative transfer model.
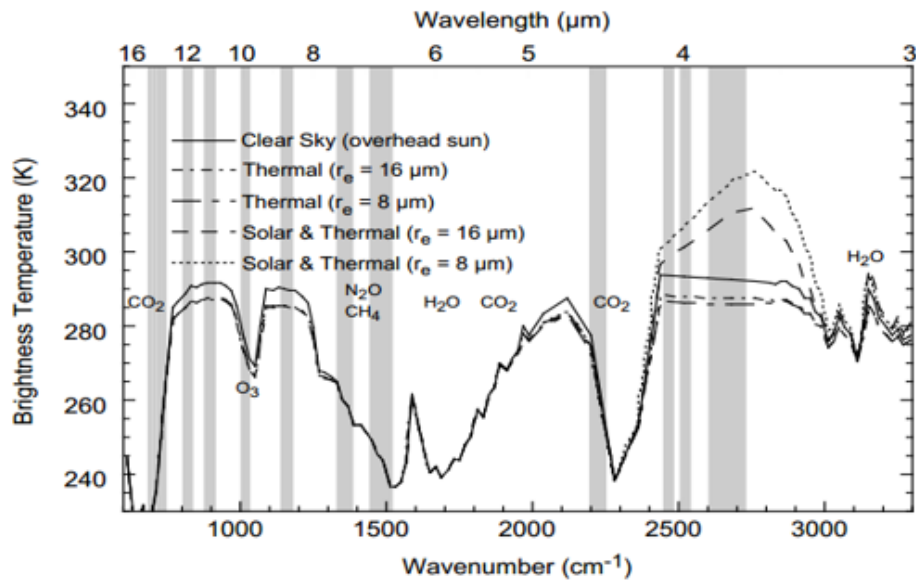
Figure. 10 Brightness temperature as a function of wavelength for nadir abservations and for various values of the effective radius of cloud droplets, where the cloud optical thickness τc (0.75 μm)=5 for all cases [14].

These computations apply to mid-latitude summer conditions, an ocean-like surface having a temperature of 294 K, unit emissivity (zero reflectance), and overhead sun. These computations further include gaseous absorption (water vapor, carbon dioxide, ozone, and the infrared water vapor continuum) at a 20 cm-1 spectral resolution, with a low-level water cloud of optical thickness 5 (at 0.75 μm) placed at an altitude between 1 and 1.5 km.

In the 3.7 μm window, both solar reflected and thermal emitted radiation are significant, though the use of the reflectance for cloud droplet size retrieval is seen to be much more sensitive than the thermal component (note that, in either case, the thermal and solar signals must be separated to provide the desired component). CO_2 absorption is important around 4.3 μm and at wavelengths greater than about 13 μm; the MODIS bands in these spectral regions can indicate vertical changes of temperature [15].

Figure 11 shows the reflection function as a function of optical thickness and effective radius for the MODIS Airborne Simulator bands used in cloud retrieval validation studies. As previously noted, the optical thickness of a cloud depends on wavelength as well as the cloud particle size distribution n(r), as reflected in the effective radius for an illustration of the spectral dependence of τ_c, g, s and τ_c'. In order to compare the curves of Fig. 10 for various wavelengths, the optical thickness $\tau_c(\lambda)$ is scaled by $2/Q_{ext}(r_e/\lambda)$ to provide a common abscissa [roughly equivalent to $\tau_c(\lambda_{vis})$] where $Q_{ext}(r_e/\lambda)$ is the extinction efficiency factor. For the visible band, scattering is nearly conservative so that separation of the reflection function curves in Fig. 11 (a) is due to an increasing asymmetry factor with droplet size (for $r_e > \sim$ 4 μm).

For the near-infrared bands, the similarity parameter (and hence droplet absorption) increases approximately linearly with effective radius, and hence the asymptotic reflectance of a cloud decreases with increasing particle size. These figures show that the visible band contains information primarily regarding cloud optical thickness, whereas the absorbing bands eventually reach an optical

thickness where they are primarily dependent on particle size alone. A combination of visible and near-infrared absorbing bands therefore provides information on both optical thickness and effective radius.

A close examination of Figs. 11b-d also reveals that the reflection function for a single absorbing wavelength is, in general, not unique. In all near-infrared bands, an effective radius of 1 μm is seen to have the same reflection function, at some optical thickness, as some other radius. This has been observed by a number of investigators, all of whom eliminated the small droplet size on the basis of physical arguments that these small sizes do not typically occur in real terrestrial clouds (e.g., Twomey and Cocks 1989, using 1.2, 1.6 and 2.2 μm; Nakajima and King 1990, using 2.2 μm; Platnick and Twomey 1994, using 3.7 μm). Nakajima and King (1990) showed that a combination of 1.6, 2.2 and 3.7 μm bands in a single cloud retrieval should eliminate this ambiguity (multivalued solution) in the retrieved particle radius [14,15].
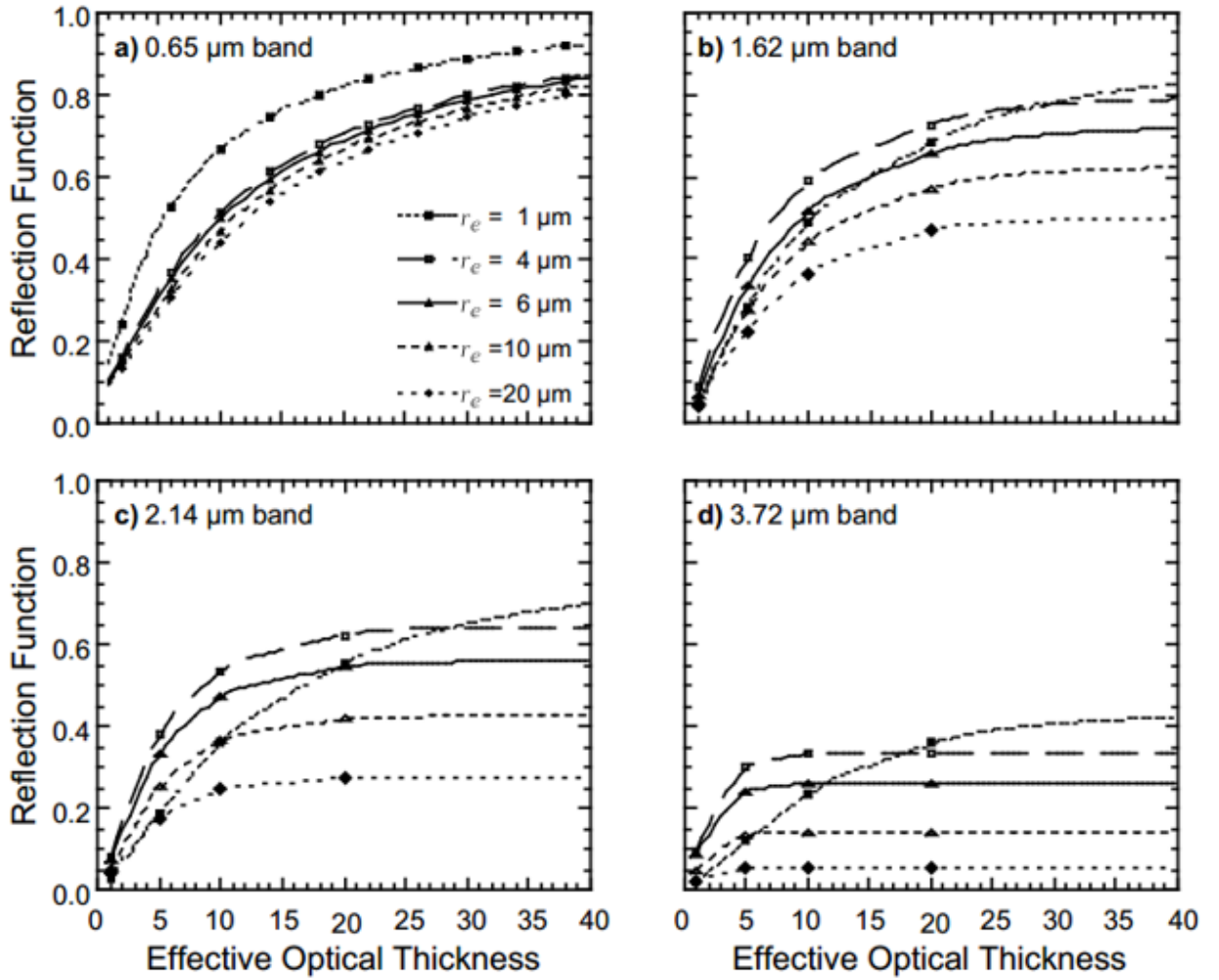
Figure 11. Reflection function as a function of optical thickness and effective radius at a visible wavelength for (a) 0.65 μm, (b) 1.62 μm, (c) 2.14 μm, (d) 3.72 μm [14].

2.11. Cloud thermodynamic phase

During the post-launch time period, we plan to perfect a robust and routine algorithm for determining cloud thermodynamic phase (water vs ice). The physical principle upon which this technique is based is the fact that the differences in reflected solar radiation between the 0.645 and 1.64 μm bands contain information regarding cloud particle phase due to distinct differences in bulk absorption characteristics between water and ice at the longer wavelength. The

visible reflectance, suffering no appreciable absorption for either ice or liquid water, is relatively unaffected by thermodynamic phase. However, if the cloud is composed of ice, or if the surface is snow covered (similar in effect to large ice particles), then the reflectance of the cloud at 1.64 µm will be smaller than for an otherwise identical liquid water cloud. The 2.13 µm band is expected to show a significant decrease in reflectance as well, but this is somewhat less dramatic than the reduced reflectance at 1.64 µm.

For added phase discrimination, it is expected that a retrieval of cloud effective radius using the 1.64 µm band alone will yield a substantially different result than one obtained using only the 2.13 µm band. As an example of the sensitivity of the 1.64 and 2.13 µm bands of MODIS to the thermodynamic phase of clouds, we have examined MAS data obtained over the northern foothills of the Brooks Range, Alaska, on 8 June 1995.
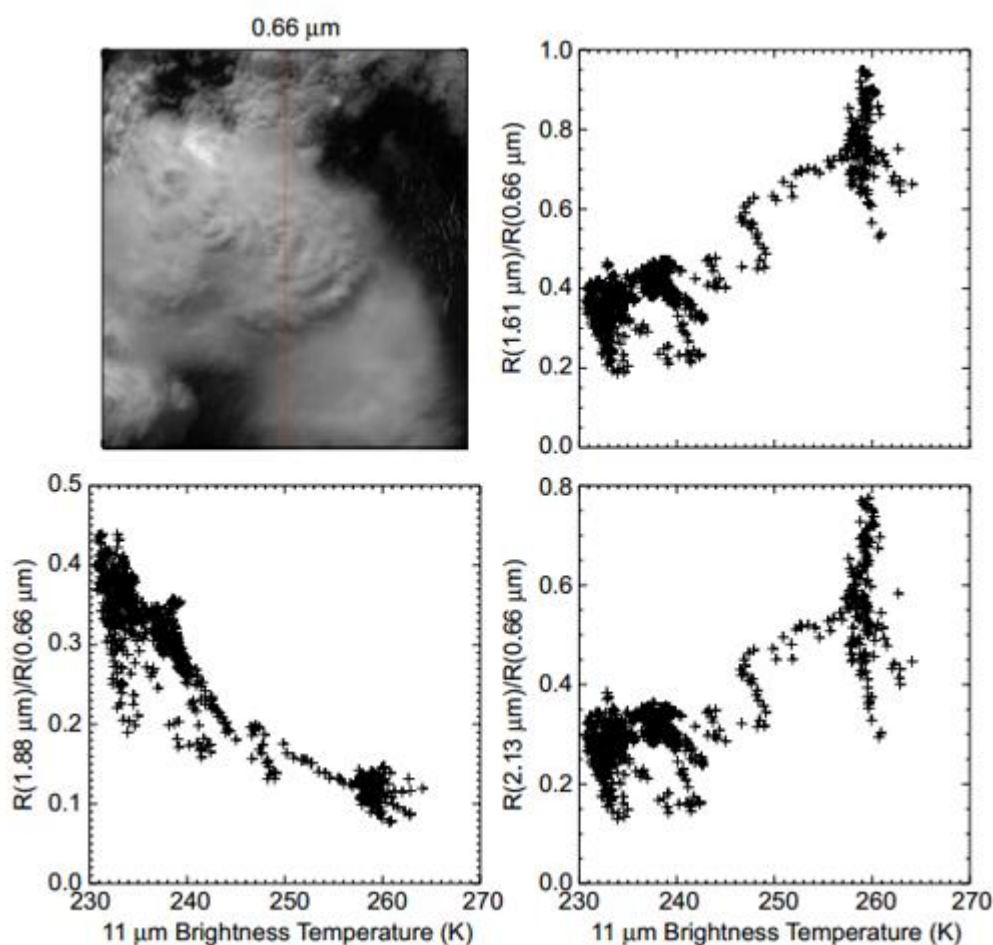
Figure 12. The upper left-hand picture shows a 0.66 μm image of a convective cumulonimbus cloud surrounded by lower-level water clouds. Others pictures show scatter plots of the reflection function ratio R(1.61)/R(0.66), R(1.88)/R(0.66), R(2.13)/R(0.66) as a function of the brightness temperature at 11.02 μm [14].

These data were acquired as part of a NASA ER-2 airborne campaign to study arctic stratus clouds over sea ice in the Beaufort Sea. The panel in the upper left portion of Fig. 12, acquired at 0.66 μm, shows high contrast between an optically thick convective cumulonimbus cloud in the center of the image, a diffuse cirrus anvil in the lower part of the image, less reflective altocumulus clouds in the upper part of the image, and dark tundra. From data obtained down the nadir track of the air craft (vertical line down the center of the image), we have produced scatter plots of the ratio of the reflection function at 1.61, 1.88, and 2.13 μm to that at 0.66 μm as a function of the brightness temperature at 11.02 μm.

These observations clearly shows that the cold portion of the scene contained ice particles (low reflectance at 1.61 and 2.13 μm), whereas the warm portion contained water droplets (high reflectance at 1.61 and 2.13 μm), as expected. In addition, the 1.88 μm band, the closest analog to the 1.38 μm water vapor absorbing band on MODIS, suggests that the colder ice clouds were high in the atmosphere (high 1.88 μm reflectance), whereas the warmer water clouds were low in the atmosphere (low 1.88 μm reflectance) [13,14, 16].

Chapter 3. Detection of Fog and Low Stratus with multispectral MODIS Data

3.1. Formation of data archive

The first phase of the working out includes the formation of the archive of the multispectral satellite images obtained by MODIS sensor, with a complex type of the underlying surface of the scene. Source of data: www.ladsweb.modaps.eosdis.nasa.gov.

Table 1. Archive of the multispectral satellite images obtained by MODIS sensor.

№	Name of product	Location	Date	Time	Satellite
1	MOD021KM.A2016184.1815.006.2016185073708	Spitsbergen archipelago	23.09.2016	07:20	Terra
2	MOD021KM.A2016185.0730.006.2016185193144	Severnaya Zemlya archipelago	20.08.2016	09:10	Aqua
3	MOD021KM.A2016250.0455.006.2016250134020	Laptev Sea	6.09.2016	06:00	Terra
4	MOD021KM.A2016263.0605.006.2016263192915	Kara Sea	19.09.2016	06:05	Aqua
5	MOD021KM.A2016251.0225.006.2016251215413	East Siberian Sea	06.09.2016	04:00	Terra
6	MOD021KM.A2016246.1015.006.2016246192721	The Taymyr Peninsula	01.07.2014	6:20	Terra
7	MOD021KM.A2016247.0605.006.2016248004328	Gulf of Ob (Obskaya guba)	07.09.2016	03:15	Aqua
8	MOD021KM.A2016248.0330.006.2016248133004	Delta Of Lena river	04.09.2016	03:30	Terra

3.2. Geographic binding

Based on the theoretical information satellite image of the Arctic seas were selected, especially for July, August and September 2013-2016. The searching of satellite imagery with the presence of fog should be guided by the characteristic structure and texture of the fog. Fog is differ by matte texture, bright white, and ragged or sharp edges or the contours repeat of the coastline.

For example, the satellite images with advective fog and low stratus clouds over the surface of the sea were gained on Sep 6th 2016 over the Laptev sea in the morning hours.

Geographical binding is carried out to determine the precise location of the ground track on the map. It is achieved by it is establishment of the relationship between the coordinate system of the satellite image and geographical XYZ system of coordinates in the selected projection using telemetry data.

Figure 13 shows the geographic coordinates of the corner and central pixels of the image. Due to the fact that there is a gap, as for most of the Polar region images it is unavailable to build up the geographic reprojection.

Center latitude	78°29'02" N
Center longitude	128°06'32" E
Upper left latitude	87°27'29" N
Upper left longitude	27°55'06" W
Upper right latitude	71°10'32" N
Upper right longitude	176°41'43" E
Lower left latitude	72°50'19" N
Lower left longitude	73°27'10" E
Lower right latitude	64°33'06" N
Lower right longitude	129°50'25" E
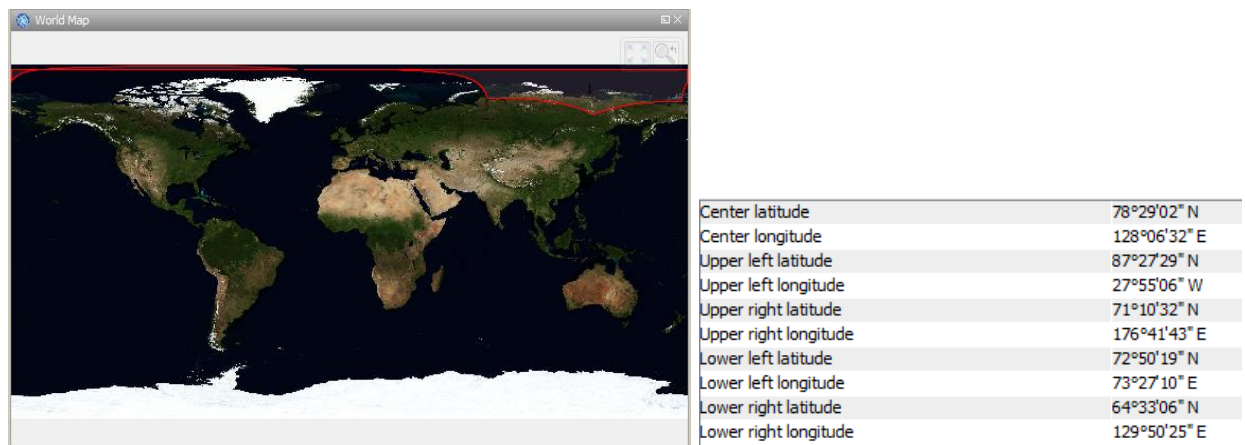
Figure 13. Location on the Earth and coordinates of used satellite image.

3.3. Selection of informative bands

Remote sensing in visible and near-infrared bands is based on the detection of the solar radiation reflected by the objects according to their spectral reflectivity. Figures show the optical characteristics of objects — their spectral brightness. Lighting is needed for shooting, and cloud cover in this case prevents shooting. Sensing in the thermal infrared range to determine the temperature of the underlying surface is based on the measurement of own thermal radiation of the surface. Shooting in this range does not depend on the illumination, can be performed over night, but the clouds and here are the hindrance.

The theoretical rationale for the selection of informative bands is based on different characteristics of reflectivity and emissivity of the cloud particles with different effective radius (the effective radius, i.e. the radius of the drops, giving the maximum contribution to the water content), that is necessary to develop models for selected bands with the most pronounced differences in these characteristics.

The greatest differences of brightness temperatures at different values of the effective radius are observed at 3.9, 8.7, 10.8, 12 μm. The greatest differences of spherical albedo at different values of the effective radius are observed at 0.8, 1.6 , 2.1, 3.9 μm.
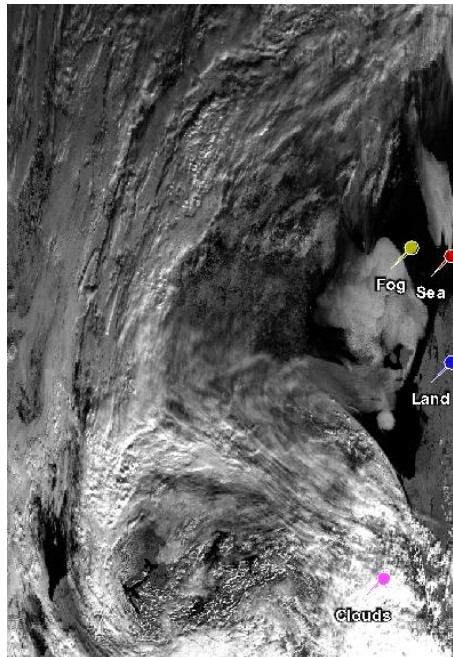
Figure 15. Fog over the Laptev sea at 0.8 μm band with marks.
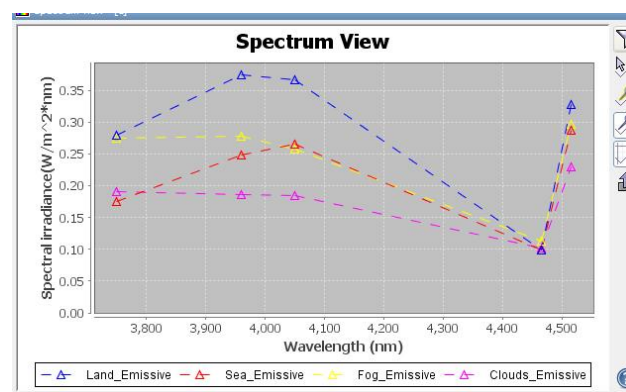
Figure 16. Spectrum view of satellite images in range 3.7 μm -4.5 μm
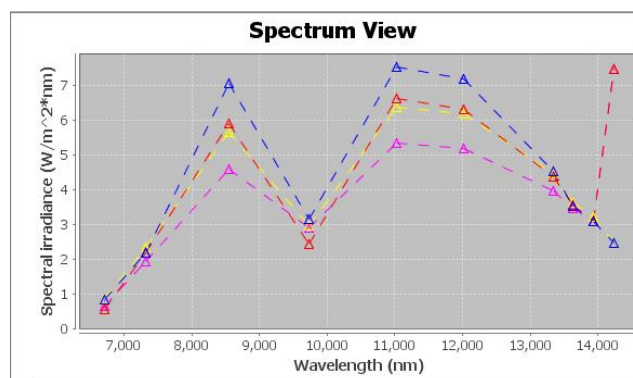
Figure 17. Spectrum view of satellite images in range 6.7 μm -14.2 μm
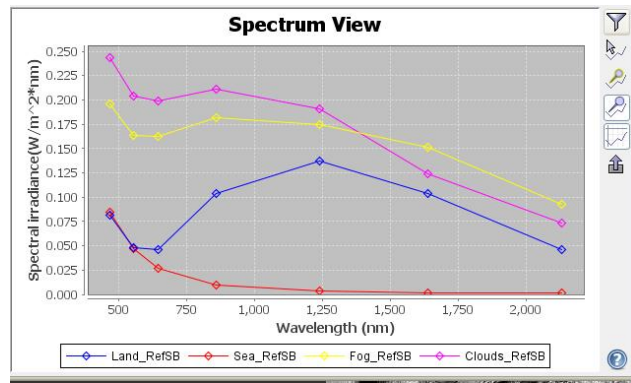
Figure 18. Spectrum view of satellite images in range 0.6 µm -2.5 µm

3.4.   Thematic processing of satellite images

The second phase of the work includes the development of models of additive color synthesis using the RGB model for accurate interpretation of fogs and low stratus clouds.

Scatterplots are used to demonstrate the presence or absence of correlation between two variables. In this case, it is constructed to show how different the images in the brightness in the selected bands. For each band, the value range is evenly divided into 512 bins. The scatter plot shows these bins plotted against each other, resulting in 512*512 cells. For each cell, the number of pixels within the according bands' value ranges is counted and color coded. Yellow stands for large amounts of pixels, black for small ones. If no pixel is assigned to a distinct cell, the cell will receive no color.
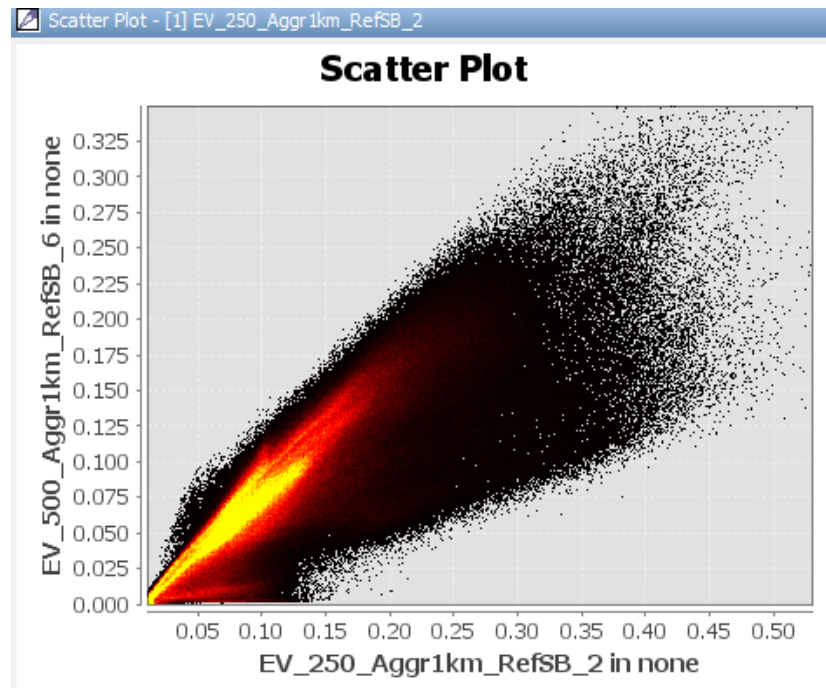
Figure 19. Scatter plot of images at O. 8 and 1.6 μm.

Scatter plot (Fig. 19) has the form of a wide sheet and a lot of black dots, suggesting substantial differences in the values of the integral brightness of the images in the selected bands (and thus the digital data processing is not required, visually the images in different bands are different, see Fig. 20 (a,b))

The satellite images of Lena Delta on 04.09.2016, 03:30 UTC.

Figure 20 (a). Satellite image

at 0.6 µm
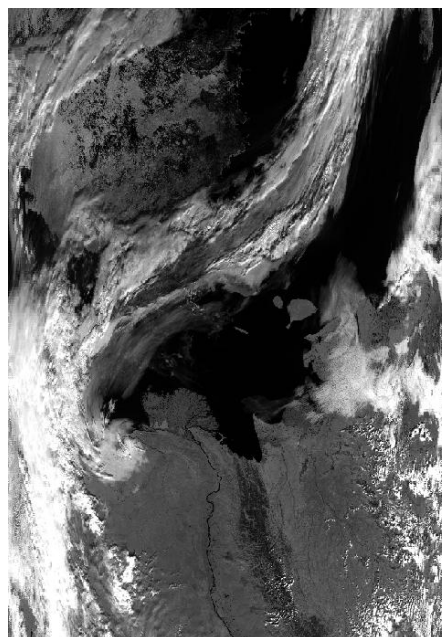
Figure 20 (b). Satellite image

 at 0.8 µm
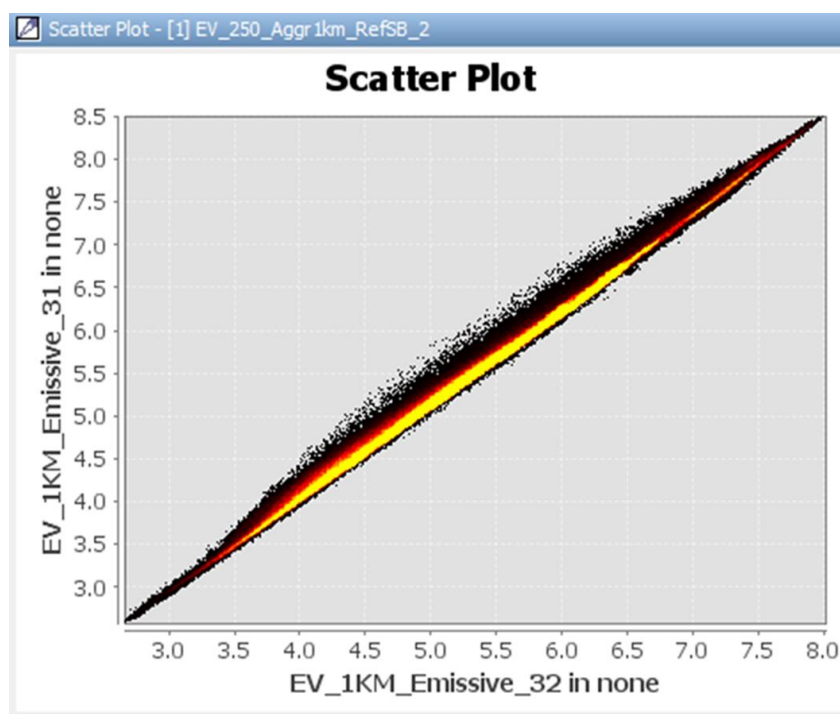
Figure 21. Scatter plot of images at 11 and 12 µm.

Scatter plot   (Fig. 21) has the form of a narrow sheet, suggesting insignificant differences in the values of the integral brightness of the images in the selected bands (11 and 12 μm), and thus the digital data processing is required.

Digital processing emphasize the difference of brightness between images in the analyzed bands, which is not visible to the naked eye, for example, Figure 22 (a-c).
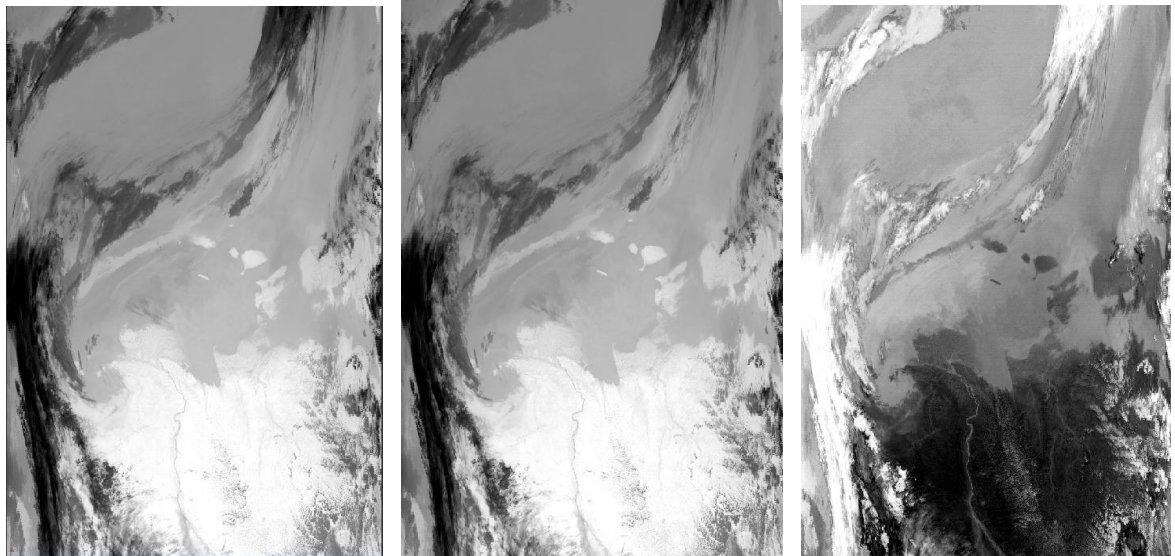
Figure 22 (a). Satellite image at 11 μm   Figure 22 (b). Satellite image at 12 μm   Figure 22 (c). Satellite difference image(12-11)

The examples of scatter plots for the other selected bands are given in Appendix B.

3.5.   Synthesis of color images.

The process of synthesis is to display a grayscale satellite images corresponding to different bands in red, green or blue color to emphasize the relative contrasts between the bands.

Analysis of objects according to multiple spectral bands is often carried out in the space of spectral signs. If the brightness values in n-dimensional variety is postponed on the coordinate axes we will get the p-dimensional space of spectral features. In this space objects are represented as groups of points. The dimension of this space depends on the number of the compared spectral ranges. To describe the standard colors of the International Commission of Illumination developed color models. Each color model defines the space within a coordinate system in which each color is represented a single point.

Various models are used to describe colors, with the RGB color model being the one used to produce the colors that we see in electronic devices such as televisions and computer monitors.

The RGB model has three primary colors: red, green, and blue. By combining them in various ways, we get a broad array of colors, from the secondary colors of yellow, magenta, and cyan, to the grays, black, and white. Understanding how these colors are made is important for producing and interpreting RGB products.
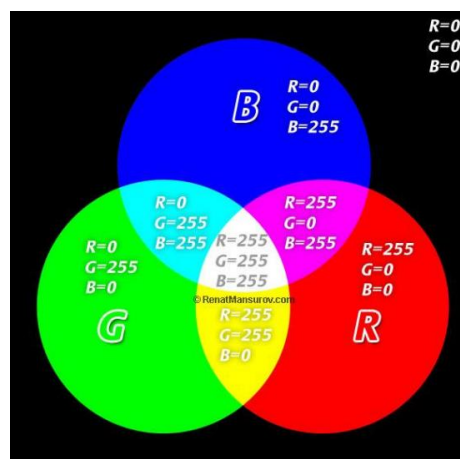
Figure 23. RGB-model.

This diagram shows how the primary colors are combined into the secondary colors, with white at the very center. In summary:

- The primary colors are red, green, and blue
- The secondary colors are:
  - Yellow, made by mixing red and green
  - Cyan, made by mixing green and blue
  - Magenta, made by mixing red and blue
- Gray is made by mixing equal amounts of three colors (other than just the primary colors)
- White is made by mixing the three primary colors in maximum amounts
- Black is the absence of the primary colors

RGB - model conveys information that would be difficult or time consuming to assess from one or more individual satellite images. To the extent possible, the product should be unambiguous and use intuitive colors to help highlight important meteorological and surface features.

The true color RGB is constructed from the three visible wavelengths that correspond to the red, green and blue components of visible light. The first spectral channel is assigned to be red, the second channel green, and the third channel blue.

Generally it is made from three or more individual or differenced spectral channels; each is assigned to a primary color (red, green, or blue); the final product highlights atmospheric and surface features that are hard to distinguish with single channel images alone. It provides intuitive, realistic looking products that can reduce ambiguities and simplify interpretation. In some situations, different features can have the same color or the same feature can appear in different colors. One way to handle this is to animate the products.

The process of building RGBs (see Fig.24)

- Step 1: Determine the purpose of the product
- Step 2: Based on experience and available scientific information, select three appropriate channels or channel derivatives that provide useful information

- Step 3: Pre-process the images as needed to ensure that they provide or emphasize the most useful information

- Step 4: Assign the three spectral channels or channel derivatives to the three RGB color components

- Step 5: Review the product for appearance and effectiveness; revise or tune as needed
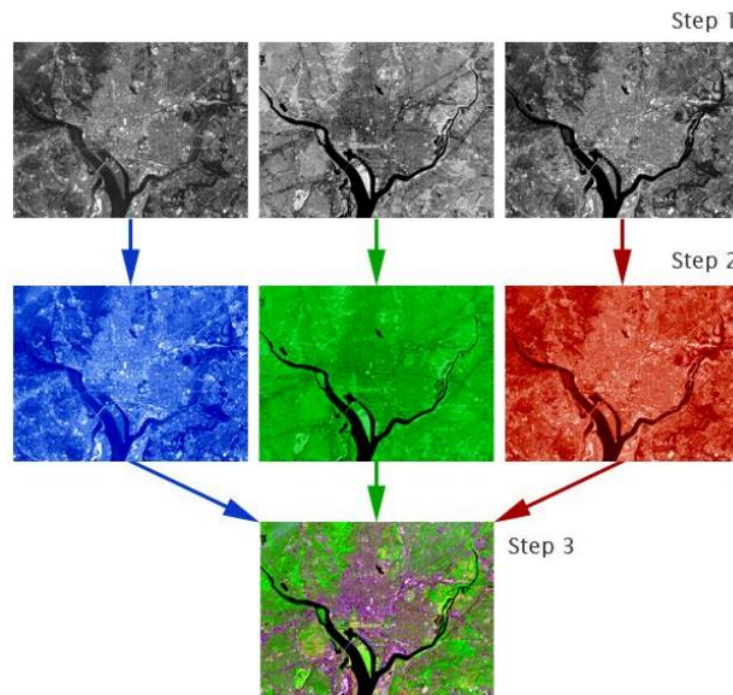
Figure 24. Color image synthesis

Example of RGB 1.6, 0.8, 0.6 combination.

Figure 25. Color image synthesis (The Gulf of Ob (Obskaya guba) 03.09.2016, 06:05 UTC) for RGB 1.6, 0.8, 0.6 combination.
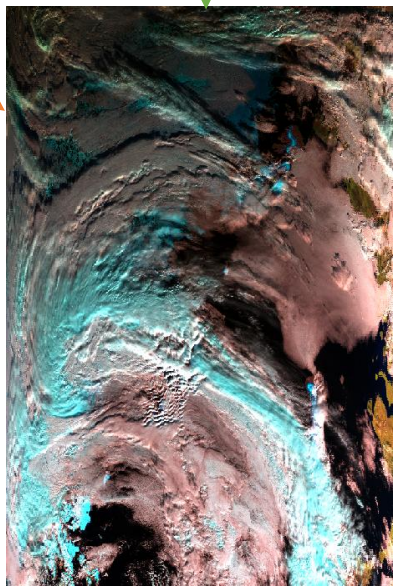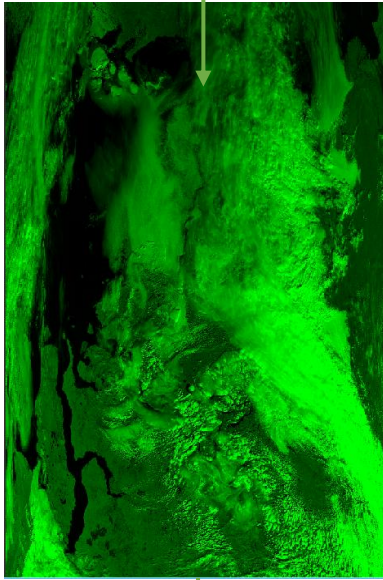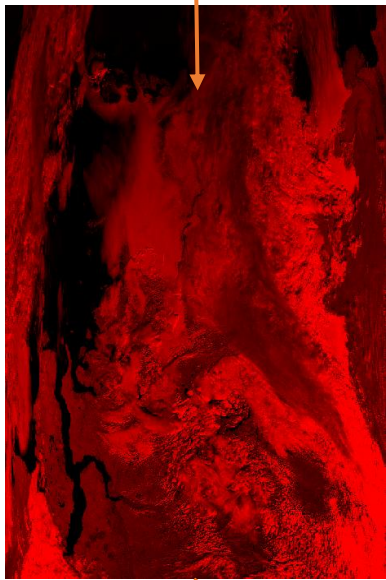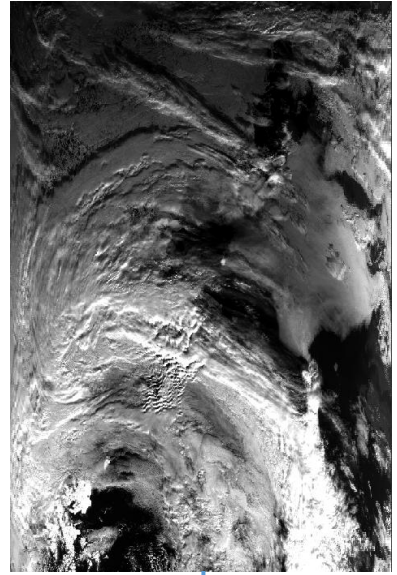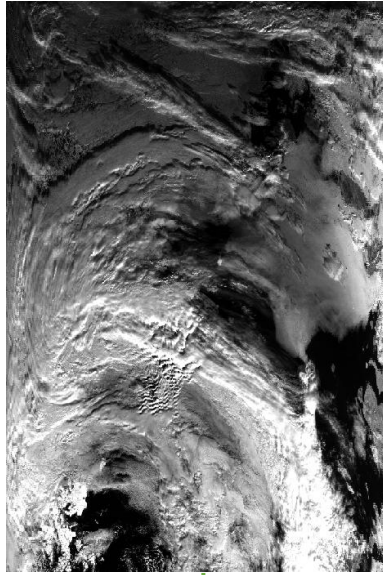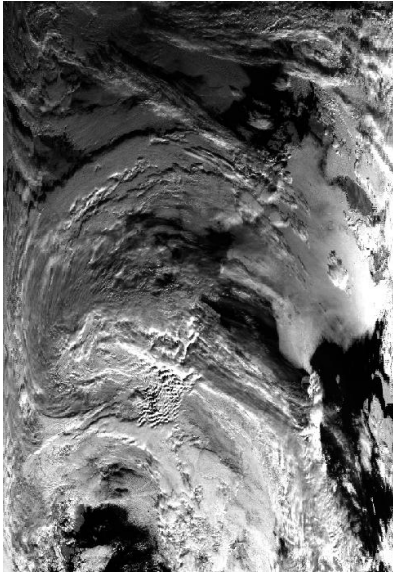
3.6. Analyses of processed satellite images

Because at the preliminary stage of work four bands has been selected, then the following four RGB combinations were created:

1) RGB (1.6, 0.8, 0.6 μm),

2) RGB (0.8, (3.9-8.7), 10.8 microns),

3) RGB (0.8, 1.6, (3.9-8.7) μm),

4) RGB ((0-12)-(0-11), ((0-11)-(0-3.8)), (0-11) microns).

For receiving of the color images overlap each other three-band multispectral image coding as its colors. If these three grayscale images to write to those areas of memory that control the intensity of red, green and blue dots (luminophors) of the screen, then it could be received a color image in natural colors.

The satellite images with advective fog and low stratus clouds over the Laptev sea on Sep 6th 2016, 06:00 UTC after digital processing and color image synthesis were reviewed.

The image obtained by using scheme No. 1 (RGB 1.6, 0.8, 0.6) helps to ensure that it is fog (Fig. 26 (a)).

When using this scheme the warm clouds to liquid-drop phase the objects are pink. Ice clouds and snow have a turquoise color. Since, this scheme uses the 1.6 μm channel in order to distinguish the ice cloud, snow and ice on the earth's surface.
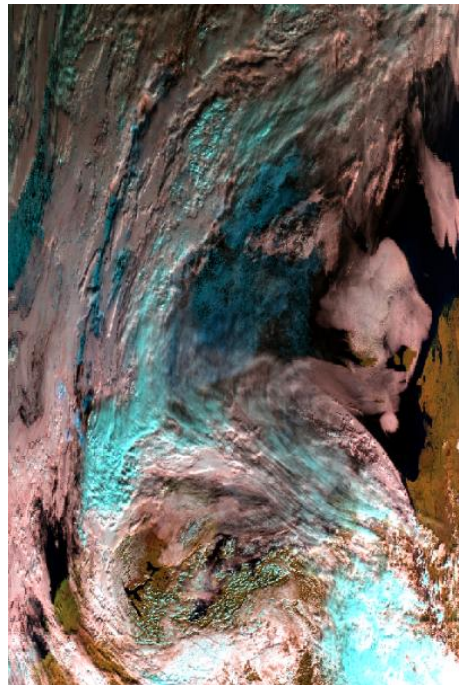
Figure 26(a). RGB 1.6, 0.8, 0.6
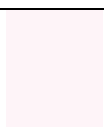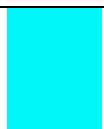
Object	Red IR 1.6	Green IR 0.8	Blue IR 0.6	RGB	Color
Fog	199	138	134	#c78a86	
Low-level clouds	218	164	165	#daa4a5	
Middle-level clouds	251	244	248	#fbf4f8	
Upper-level clouds	107	247	249	#6bf7f9	
Ice	12	85	106	#0c556a	

Table 2. Tables of color compliance for RGB 1.6, 0.8, 0.6

The image obtained by using scheme No. 2 (RGB 0.8, (3.9-8.7) 10.8) also helps to ensure that it is fog (Fig. 26 (b)). When using this scheme the warm clouds to liquid-drop phase the objects are purple. Ice clouds and snow are green.
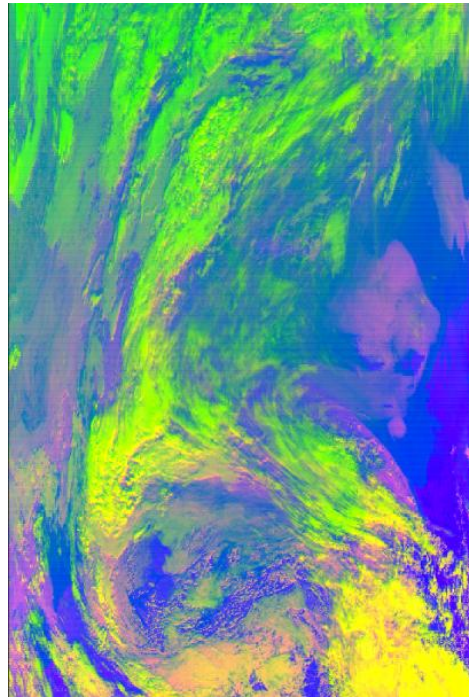
Figure 26 (b). RGB 0.8, (3.9-8.7) 10.8
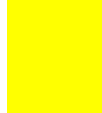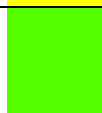
Object	Red IR 0.8	Green IR 3.9-8.7	Blue IR 10.8	RGB	Color
Fog	145	100	104	#9164cc	
Low-level clouds	242	156	140	#f29c8c	
Middle-level clouds	255	255	0	#ffff00	
Upper-level clouds	158	255	0	#9eff00	
Ice	107	159	138	#6b9f8a	

Table 3. Tables of color compliance for RGB 0.8, (3.9-8.7) 10.8

Then scan the image using scheme No. 3 (RGB 0.8, 1.6, (3.9-8.7)), under this scheme, the warmest objects are the objects of green color. The cold – purple. The result is shown in Fig. 26 (c).
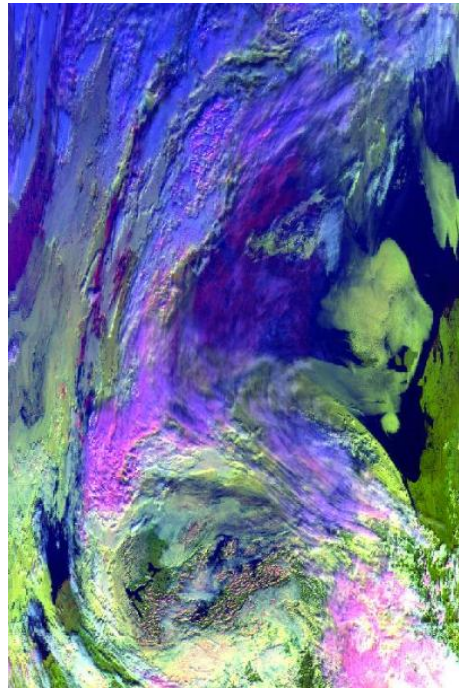
Figure 26 (c). RGB 0.8, 1.6, (3.9-8.7)

Object	Red IR 0.8	Green IR 1.6	Blue IR 3.9-8.7	RGB	Color
Fog	155	203	94	#9bcb5e	
Low-level clouds	115	173	171	#73adab	
Middle-level clouds	156	105	255	#9c69ff	
Upper-level clouds	255	108	255	#ff80ff	
Ice	111	3	112	#6f0370	

Table 4. Tables of color compliance for RGB 0.8, 1.6, (3.9-8.7)

Scheme No.4 (RGB ((0-12)-(0-11), ((0-11)-(0-3.8)), (0-11)) was created with inversion of bands 11 μm and 12 μm, the warmest objects are greyish blue, the coldest-bright blue. The result is shown in Fig. 26 (d).
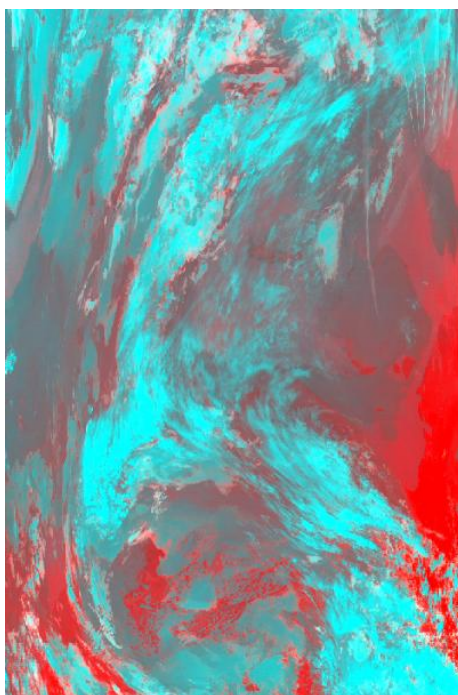
Figure 26 (d). RGB (0-12)-(0-11), (0-11)-(0-3.8), (0-11)

Object	Red IR-12-(-11)	Green IR-11-(-3.9)	Blue IR-11	RGB	Color
Fog	135	96	99	#876063	
Low-level clouds	118	126	130	#767e82	
Middle-level clouds	87	173	174	#57adae	
Upper-level clouds	0	255	255	#00ffff	
Ice	79	201	201	#4fc9c9	

Table 5. Tables of color compliance for RGB (0-12)-(0-11), (0-11)-(0-3.8), (0-11).

Analysis of the obtained images has showed that the developed model of color synthesis are complementary under different conditions of implementation of the satellite shooting. In case of the fog happens over the Laptev sea (6th of September 2016 6:00 UTC) the most informative schemes are scheme № 2 and №3. In case of the fog happens over the The East Siberian Sea (6th of September 2016 4:00 UTC) the most informative schemes are scheme № 1 and №4. In case of the fog happens over The Taymyr Peninsula (1st of July 2014 6:20 UTC) the most informative schemes are scheme №1 and №3 (see Appendix D).

Therefore, during the detection of fog and low stratus clouds in the case of complex underlying surface, it is advisable to use all of the developed scheme.

Conclusion

In the process of implementation of the present qualification work the following results and conclusions have been got.

The first chapter is denoted to the conditions of various types of fog and low stratus clouds over the Arctic seas. Some brief characteristics of all types of fog are described. In addition, the work also pays special attention to the possible consequences of flying in the zone of fog and low stratus location.

The second chapter claims about the principle of operation of satellite equipment for sensing the misuse of the objects, which are researched, i.e., fog and low stratus clouds and their microphysical regularities. Microphysical and spectral characteristics of the fog are studied in detail, according to the fact that in some channels of the spectrum the particles with different effective radius have the most different reflective and emissive abilities. On the basis of that processing of satellite images have been carried out, using the program Beam VISAT 5.0.

The third chapter describes the pre-processing of satellite images obtained from MODIS sensor installed on the satellites Terra and Aqua. The focus is on the development of methods of thematic processing of multispectral satellite data for program Beam VISAT 5.0, allowing to improve the quality of detection of fog and low stratus in Arctic zone. The main stages of schemes developed for additive synthesis of satellite images are: selection of informative bands through analysis of spectrograms constructed for different ranges of the electromagnetic spectrum, analysis of the scatter plots for decision on the need for additional mathematical processing of images, analysis of all possible RGB combinations based on the selected bands and the preparation the table of color correspondences for them.

In the course of work the new color schemes have been developed for distinguishing of fog and low stratus clouds accurately.

Analysis of the obtained images has showed that the developed model of color synthesis are complementary under different conditions of implementation of the satellite shooting.

To sum up, the joint use of the developed models of the color synthesis allows reliable detection of fogs and low stratus clouds in the complex underlying surfaces of the scene of the satellite imagery.

References

1. www.meted.ucar.edu

2. NASA Earth Observatory. «Landsat Goes Over the Top: A Long View of the Arctic». Accessed April 2, 2015.

3. NASA Earth Observatory, «Arctic Sea Ice». Accessed 2015.

4. Liu P. «The Effect of the Sea-ice Zone on the Development of Boundary-layer Roll Clouds During Cold Air Outbreaks» Boundary-Layer Meteorology. 2006. 118 (3), 557-581.

5. Darko Koračin, Clive E. Dorman, John M. Lewis, James G. Hudson, Eric M. Wilcox, Alicia Torregrosa. «Marine fog: A review». Desert Research Institute, Reno, NV, USA, 2014

6. Gultepe I., Liu P., Kuhn E., Pavolonis M., Calvert C, Gurka J. «Ice fog in arctic during fram-ice fog project aviation and nowcasting applications». Proquest Academic Research Library. 2014. P. 211-226

7. I. Gultepe, J.A. Mildbrandt. «Marine fog. A review on microphysics and visibility prediction». NOAA, College Park, USA, 2012.

8. Zentralanstalt für Meteorologie und Geodynamik. «Fog And Stratus – Meteorological Physical Background»Retrieved February 2009.

9. Wilfried Jacobs, Vesa Nietosvaara. «Short range forecasting methods of fog, visibility and low clouds». Office for Official Publications of the European Communities, Luxembourg, 2008.

10. Dmitriev A. V., Chimitdorzhiev T., Gusev M. A., Dagurov P. N. «Basic products of remote sensing of the Earth by space synthetic aperture radar» Federal state unitary enterprise "Scientific-publishing, printing center "Science". 2014. P.83

11. Tapakis R., Charalambides A.G. «Equipment and methodologies for cloud detection and classification: a review». Elsevier Science Publishing Company, Inc. 2013. P. 392-430

12. Maurer, John «Overview of NASA's Terra satellite». University of Hawai'i, USA, November 2001.

13. www.modis-atmos.gsfc.nasa.gov

14. Michael D. King. «Cloud retrievals Algorithms for MODIS: Optical thickness, Effective particle radius and thermodynamic phase». Version 5, 1997.

15. Lebedev A. B., Karavaev D. M., Schukin G. G. «The state and prospects of development of meteorological satellite system». State research navigation-hydrographic Institute (Saint-Petersburg). 2015. P. 31-39

16. Mehrdad Shahabi, Aung Hlaing, David R. Martinelli, Avinash Unnikrishnan. «Fog Detection for Interstate and State Highways». West Virginia University. 2012. P.68

17. www.ladsweb.modaps.eosdis.nasa.gov

Appendix A

Table 1. MODIS bands

Primary Use	Band number	Central wavelength [nm]	Bandwidth [nm]	Spatial resolution [m]
Land / Cloud / Aerosols / Boundaries	1	645	620 - 670	250
	2	858.5	841 - 876	
Land / Cloud / Aerosols Properties	3	469	459 - 479	500
	4	555	545 - 565	
	5	1240	1230 - 1250	
	6	1640	1628 - 1652	
	7	2130	2105 - 2155	
Ocean Colour / Phytoplankton / Biogeochemistry	8	421.5	405 - 420	1000
	9	443	438 - 448	
	10	488	483 - 493	
	11	531	526 - 536	
	12	551	546 - 556	
	13	667	662 - 672	
	14	678	673 - 683	
	15	748	743 - 753	
	16	869.5	862 - 877	
Atmospheric Water Vapour	17	905	890 - 920	
	18	936	931 - 941	
	19	940	915 - 965	
Surface / Cloud Temperature	20	3750	3660 - 3840	
	21	3959	3929 - 3989	
	22	3959	3929 - 3989	
	23	4050	4020 - 4080	
Atmospheric Temperature	24	4465.5	4433 - 4498	
	25	4515.5	4482 - 4549	
Cirrus Clouds / Water Vapour	26	1375	1360 - 1390	
	27	6715	6535 - 6895	
	28	7325	7175 - 7475	
Cloud Properties	29	8550	8400 - 8700	
Ozone	30	9730	9580 - 9880	
Surface / Cloud Temperature	31	11030	10780 - 11280	
	32	12020	11770 - 12270	
Cloud Top Altitude	33	13335	13185 - 13485	
	34	13635	13485 - 13785	
	35	13935	13785 - 14085	
	36	14235	14085 - 14385	

Appendix B

Location on the Earth and coordinates of used satellite image.
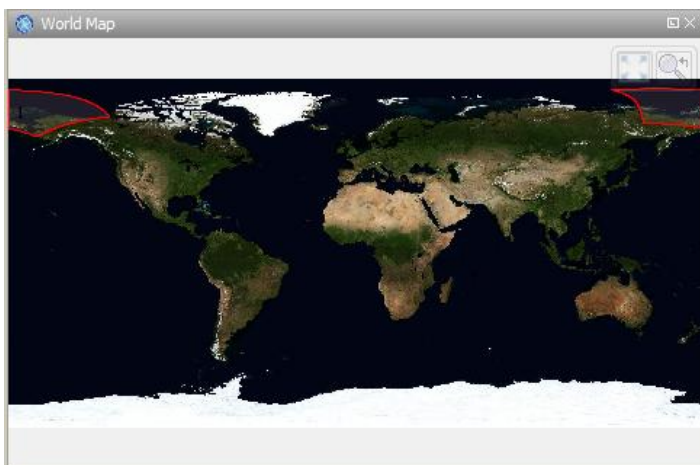
6 Sept 2016

4:00 UTC

Center latitude	73°41' N
Center longitude	173°35'15" W
Upper left latitude	84°28'34" N
Upper left longitude	132°02'13" E
Upper right latitude	70°31'35" N
Upper right longitude	127°34'46" W
Lower left latitude	66°55'48" N
Lower left longitude	148°47'30" E
Lower right latitude	60°09'16" N
Lower right longitude	165°02'20" W
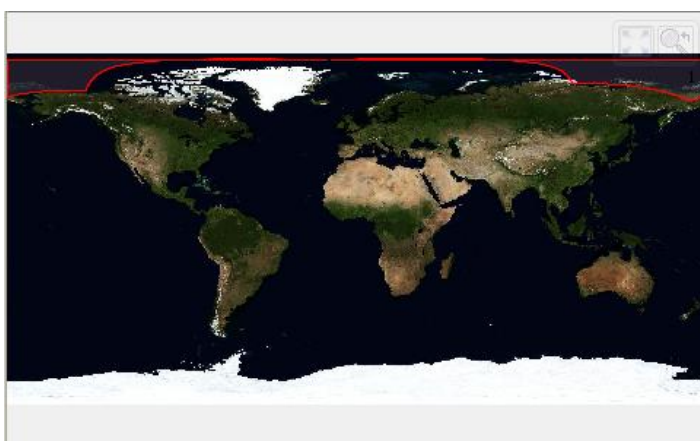
7 Sept 2016

3:15 UTC

Center latitude	79°35'42" N
Center longitude	173°30'38" E
Upper left latitude	86°29'09" N
Upper left longitude	15°03' W
Upper right latitude	71°01'06" N
Upper right longitude	139°28'40" W
Lower left latitude	74°28'56" N
Lower left longitude	111°29'25" E
Lower right latitude	65°38'17" N
Lower right longitude	171°32'59" E
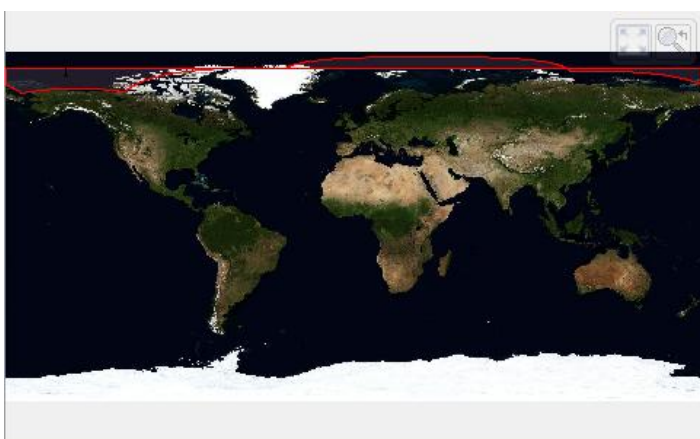
19 Sept 2016

6:05 UTC

Center latitude	72°02'36" N
Center longitude	92°04' E
Upper left latitude	82°45'30" N
Upper left longitude	46°50'09" E
Upper right latitude	69°58'08" N
Upper right longitude	135°58'15" E
Lower left latitude	65°05'14" N
Lower left longitude	57°48'24" E
Lower right latitude	58°41'15" N
Lower right longitude	101°30'24" E
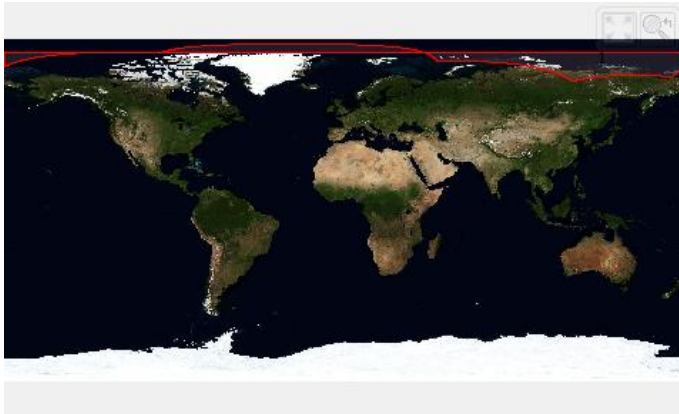
1 Jul 2014

06:20 UTC

Center latitude	81°28'05" N
Center longitude	135°25'40" E
Upper left latitude	83°00'30" N
Upper left longitude	97°19'32" W
Upper right latitude	70°04'20" N
Upper right longitude	172°03'52" E
Lower left latitude	78°24'11" N
Lower left longitude	48°48'31" E
Lower right latitude	67°58'05" N
Lower right longitude	119°40'31" E

20 Aug 2016

09:10 UTC

Center latitude	74°36'15" N
Center longitude	50°59'07" E
Upper left latitude	85°24'54" N
Upper left longitude	11°04'12" W
Upper right latitude	70°46'31" N
Upper right longitude	98°02'27" E
Lower left latitude	67°59'25" N
Lower left longitude	11°04'56" E
Lower right latitude	60°59'20" N
Lower right longitude	58°48'42" E

23 Sept 2016

07:20 UTC

Center latitude	69°19'38" N
Center longitude	69°22'43" E
Upper left latitude	79°54'28" N
Upper left longitude	33°21'25" E
Upper right latitude	68°44'44" N
Upper right longitude	109°34'22" E
Lower left latitude	62°07'39" N
Lower left longitude	39°23'30" E
Lower right latitude	56°14'17" N
Lower right longitude	79°38'52" E

Appendix C

Scatter plots for all used bands

a) Scatter plots of 0.6 μm-0.8 μm bands   b) Scatter plots of 0.6 μm-1.6 μm bands
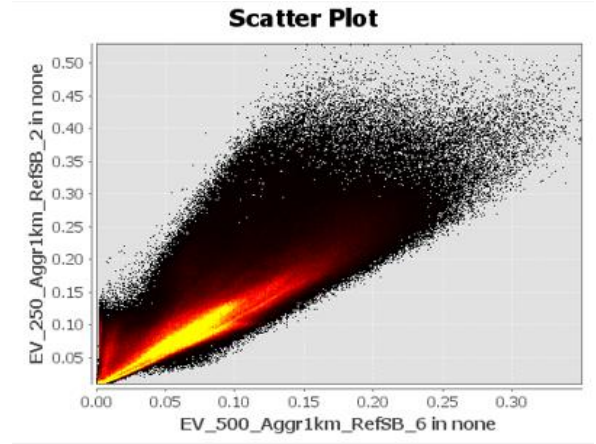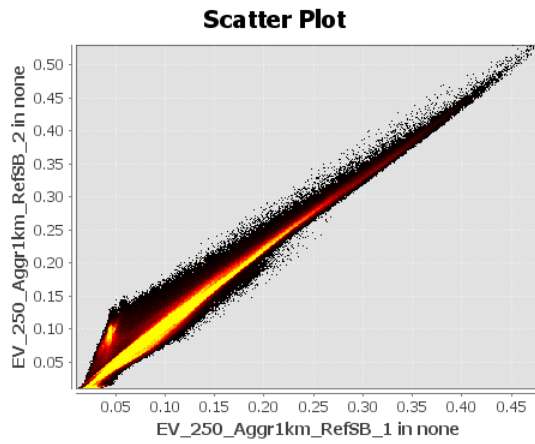
c)Scatter plots of 3.9 μm-8.7 μm bands d)Scatter plots of 3.8 μm-11 μm bands
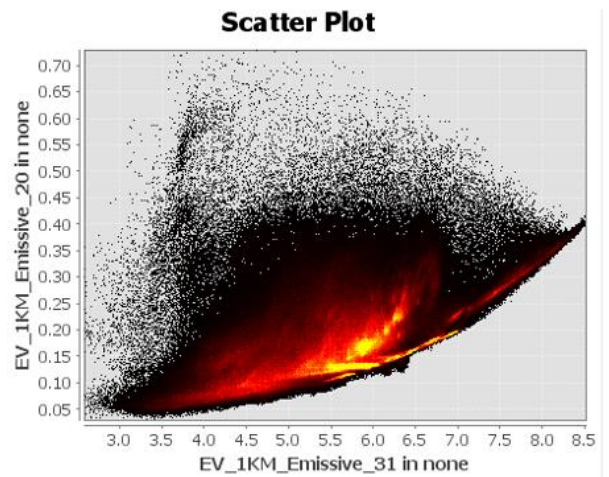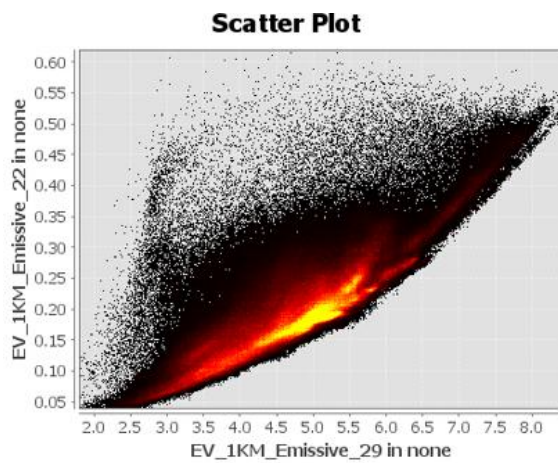
Appendix D

Satellite images in the visible spectrum with marks
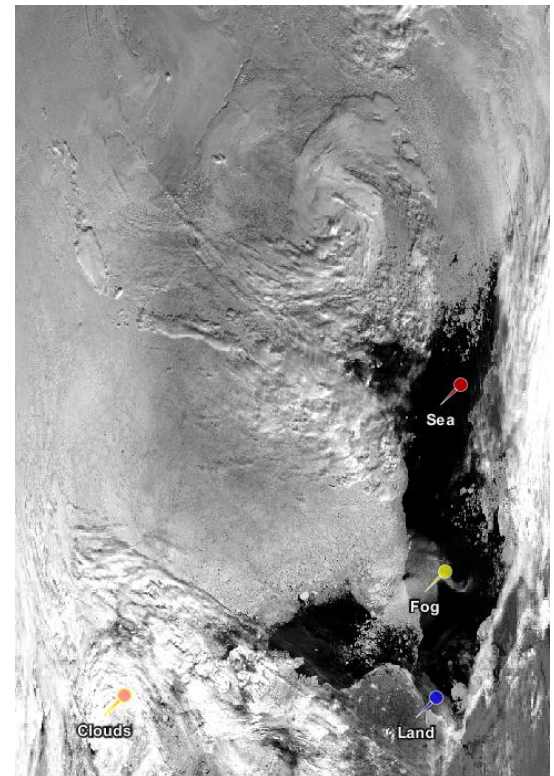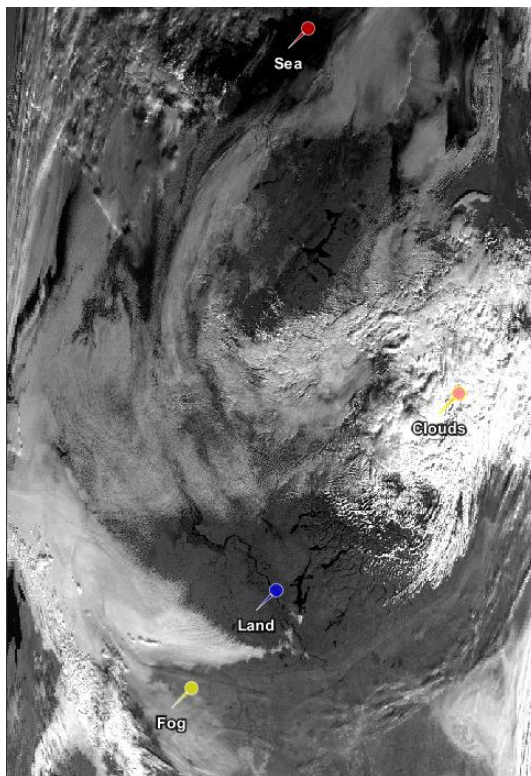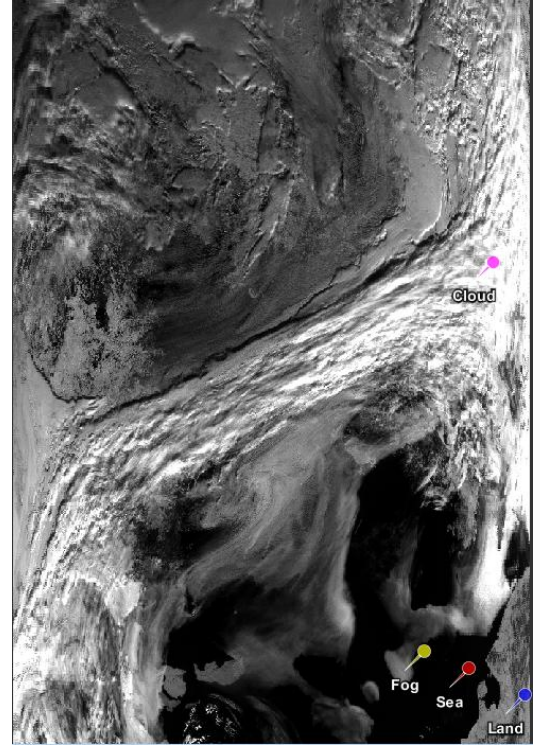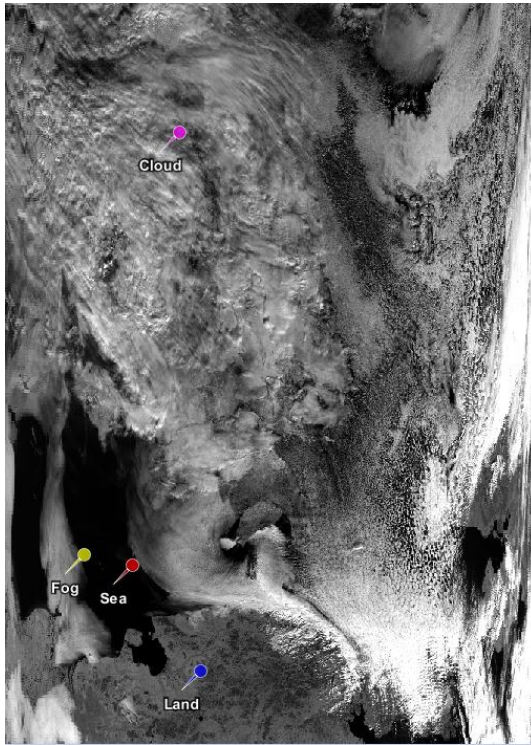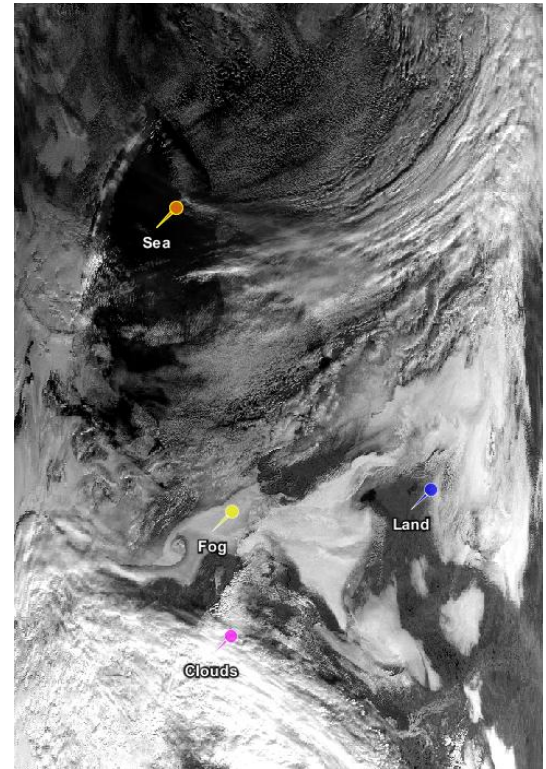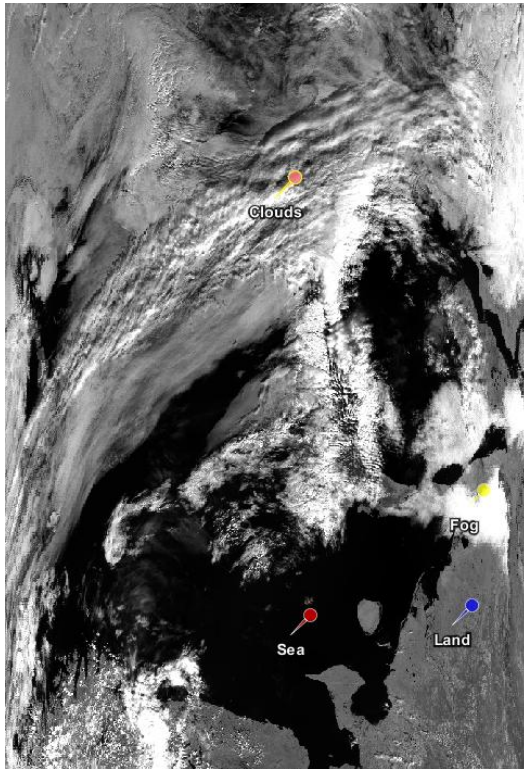
Spectrum view of all used images

a) Spectrum view of satellite images in range 3.7 μm -4.5 μm
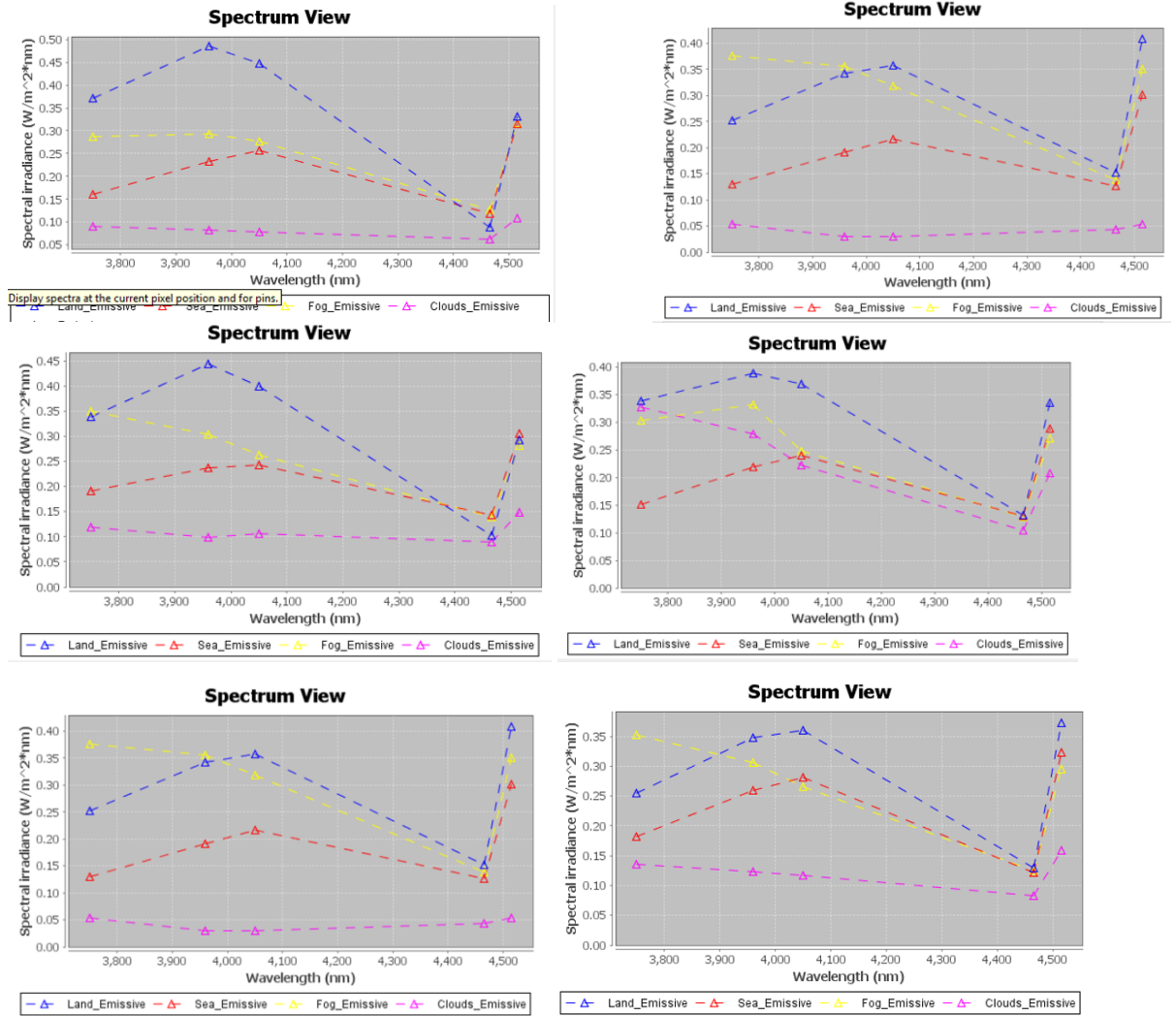
b) Spectrum view of satellite images in range 6.7 μm -14.2 μm
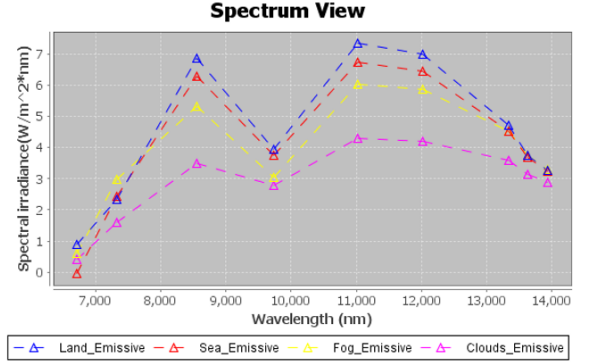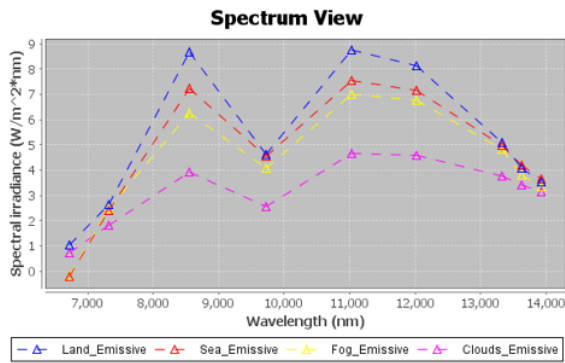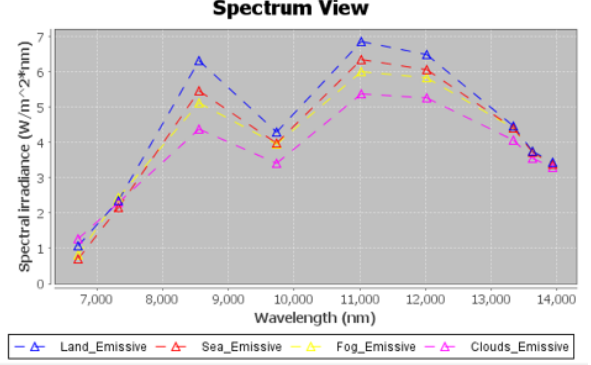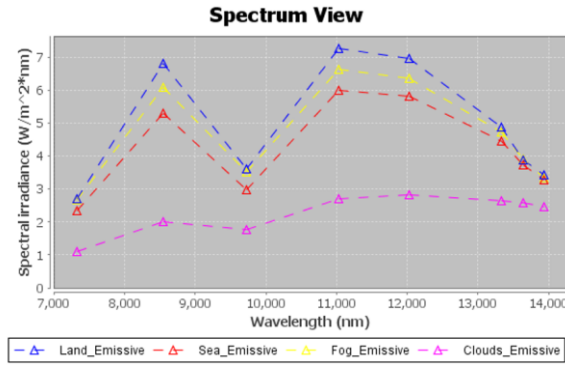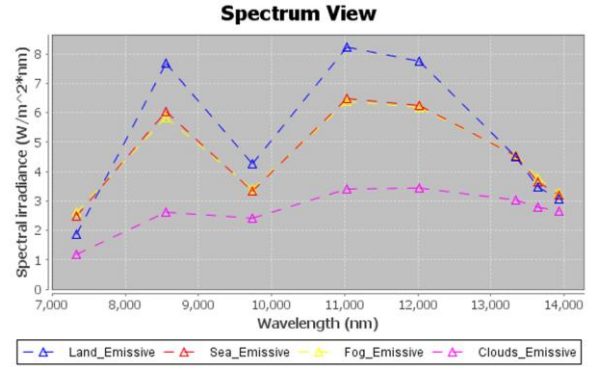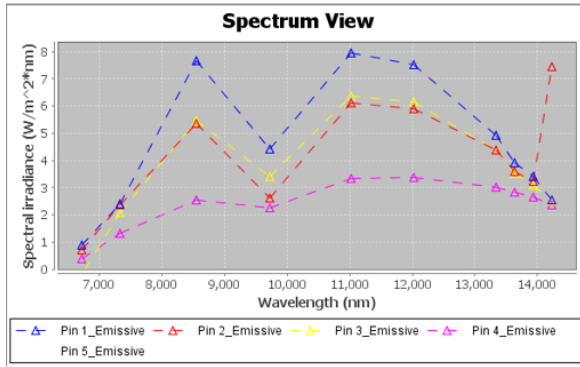
c) Spectrum view of satellite images in range 0.6 μm -2.5 μm
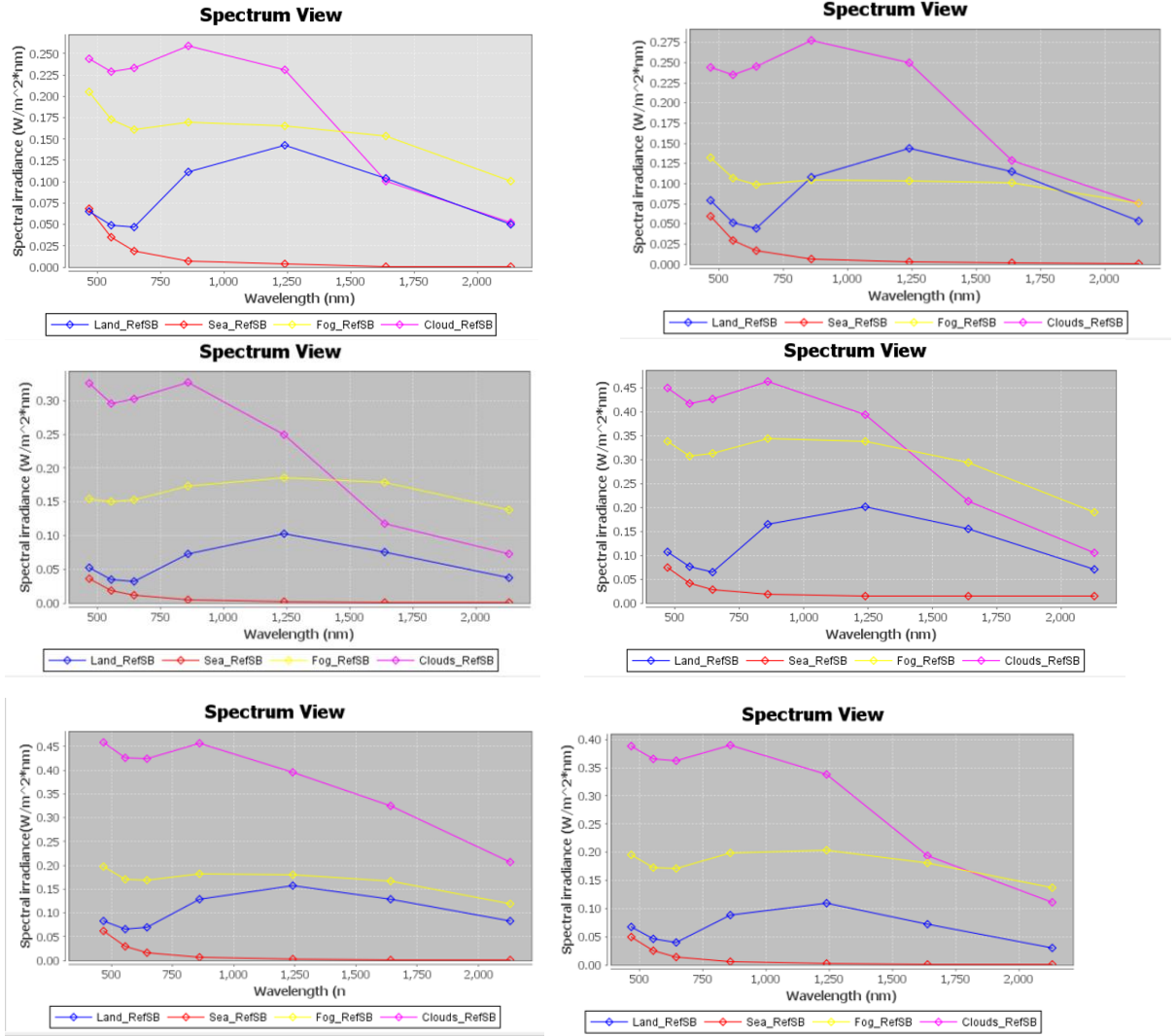
Appendix E
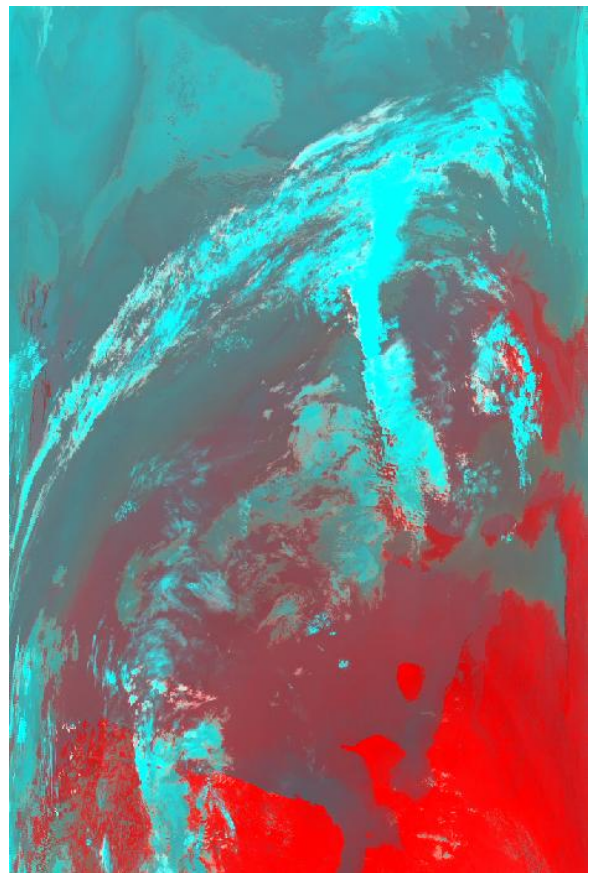
Results of thematic processing of satellite images.

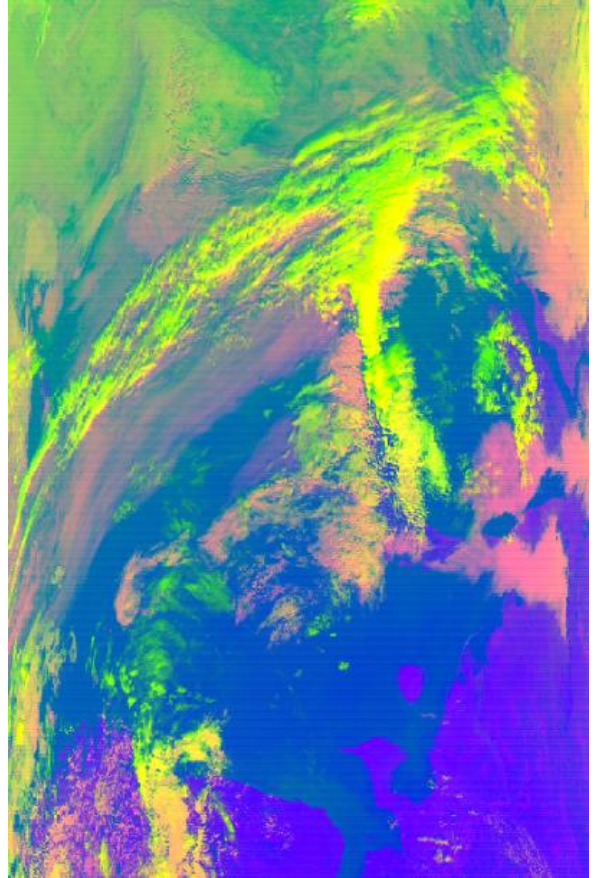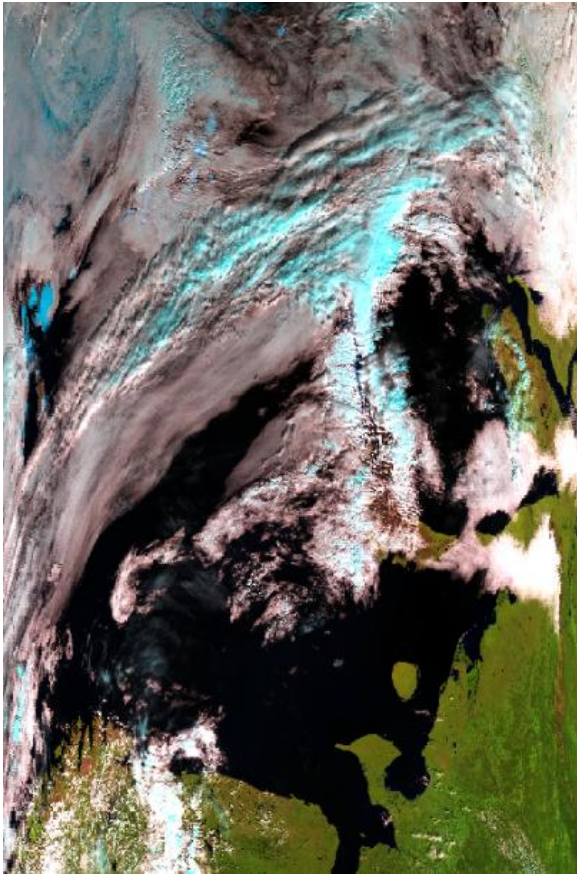Satellite images after processing (6th of September 2016 4:00 UTC)
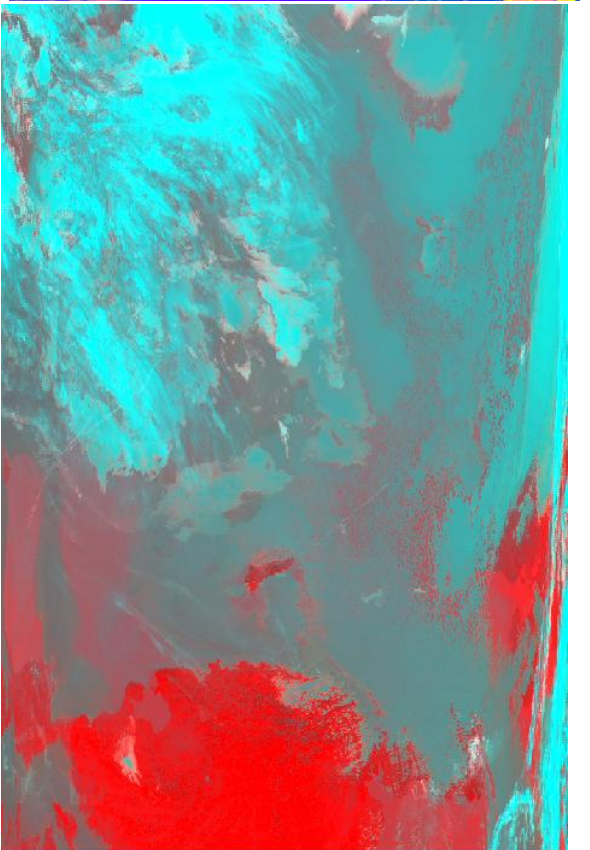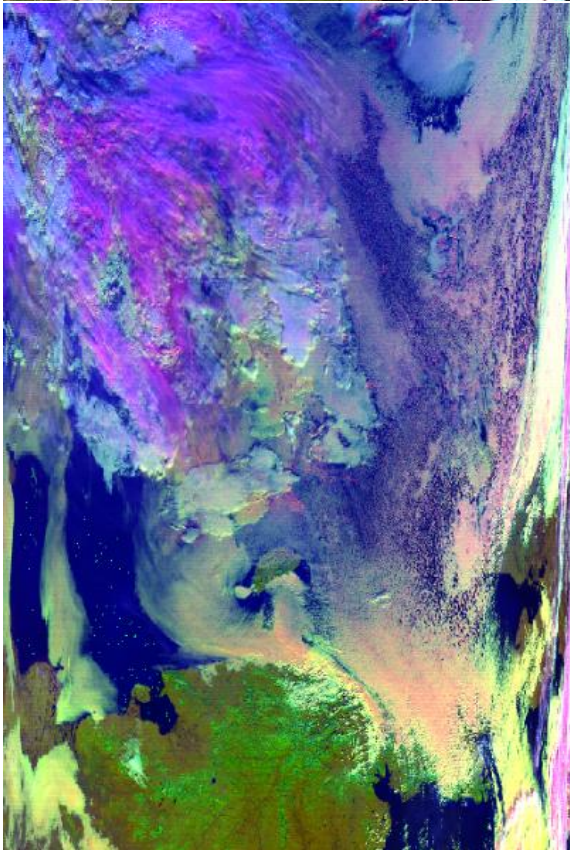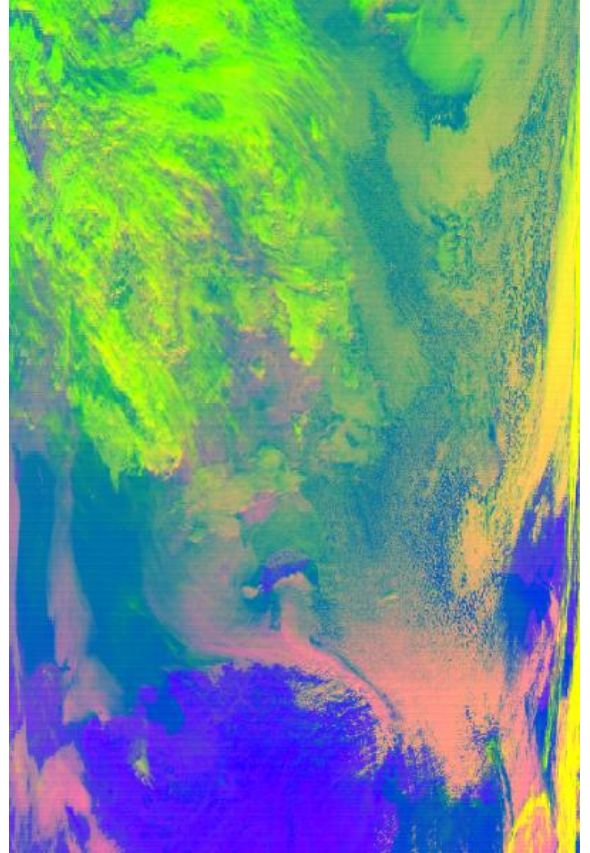
Satellite images after processing (7th of September 2016 3:15 UTC)
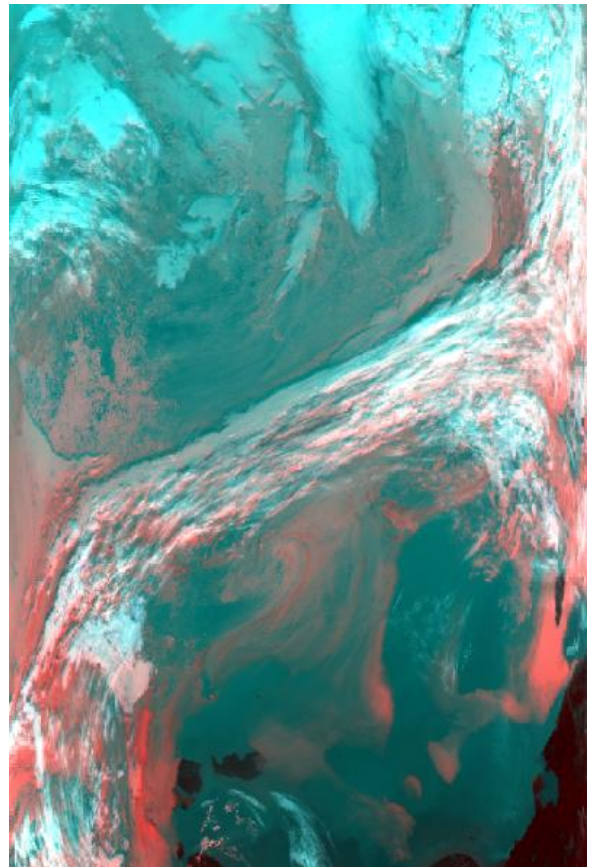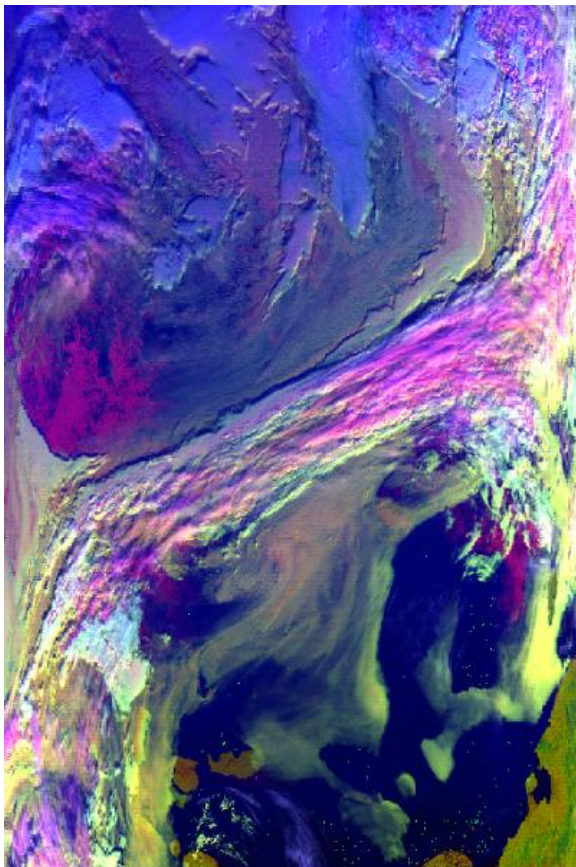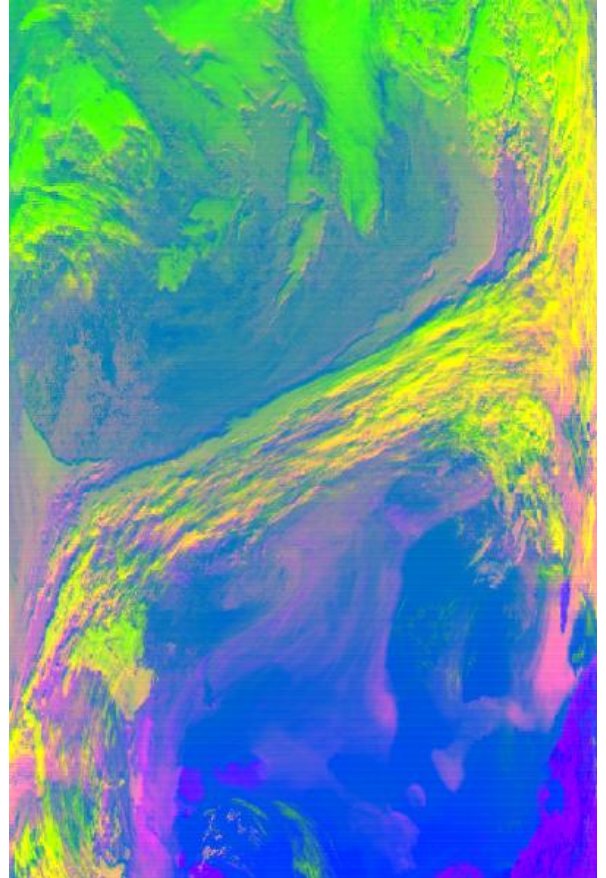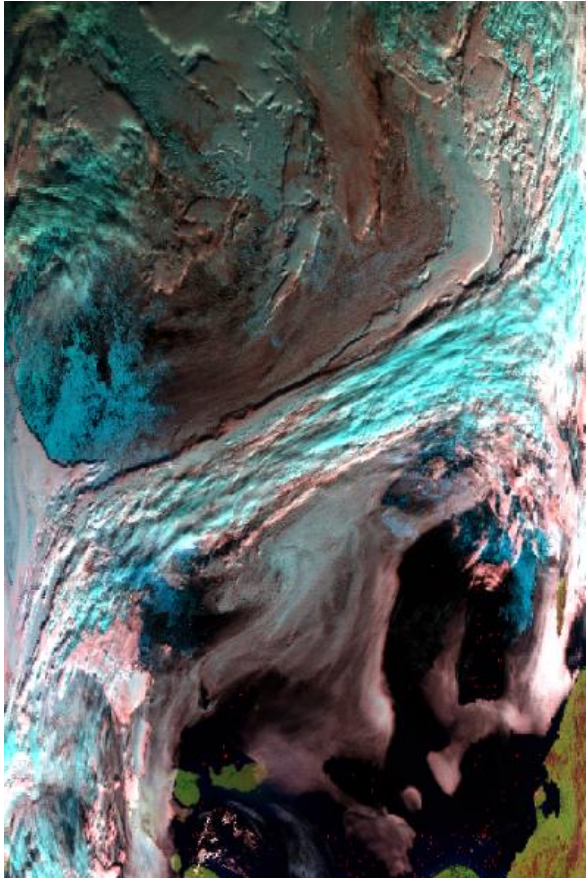
Satellite images after processing (1st of July 2014 6:20 UTC)
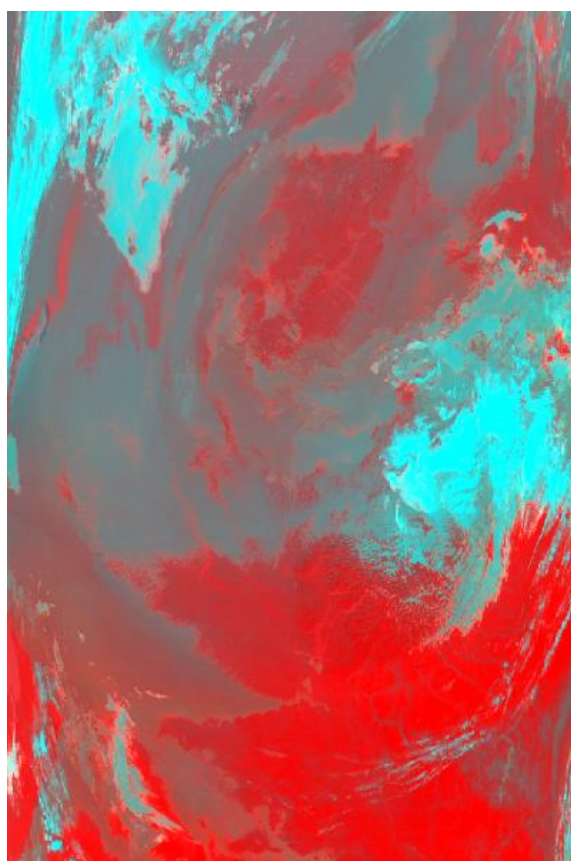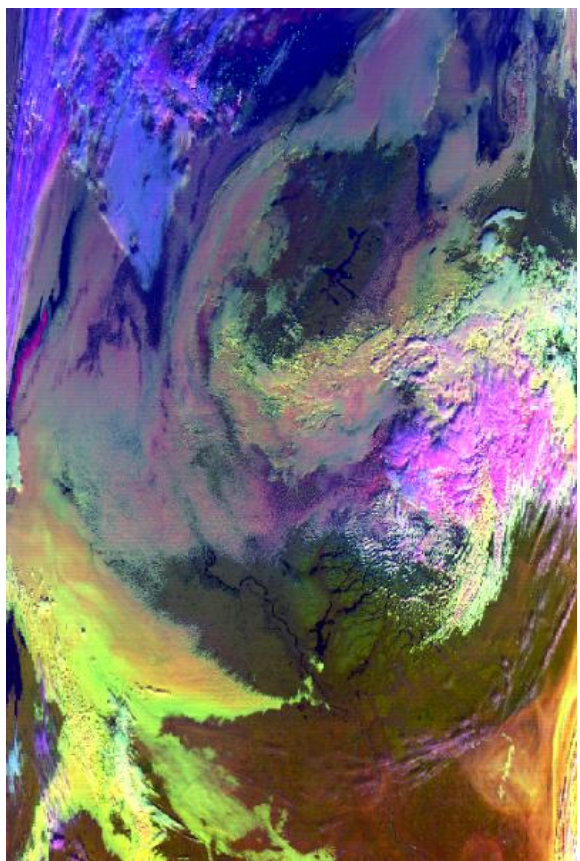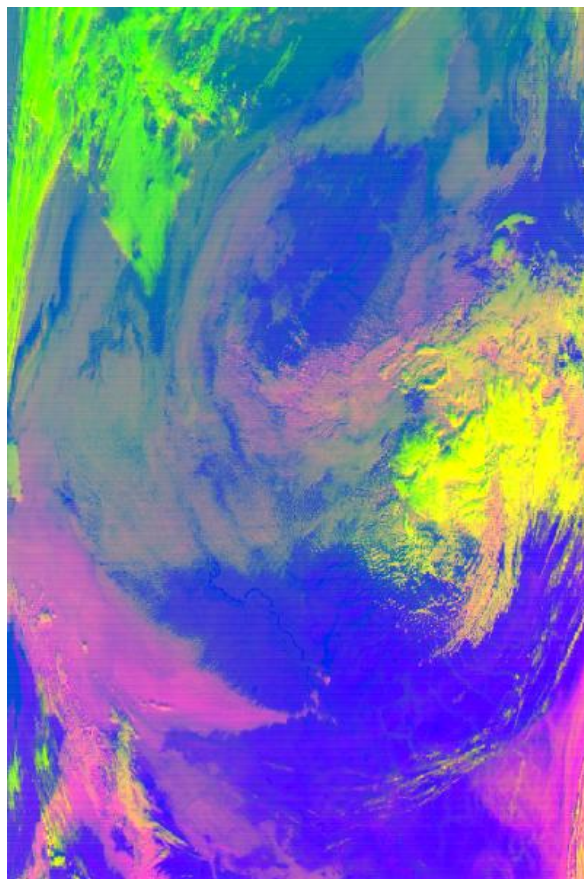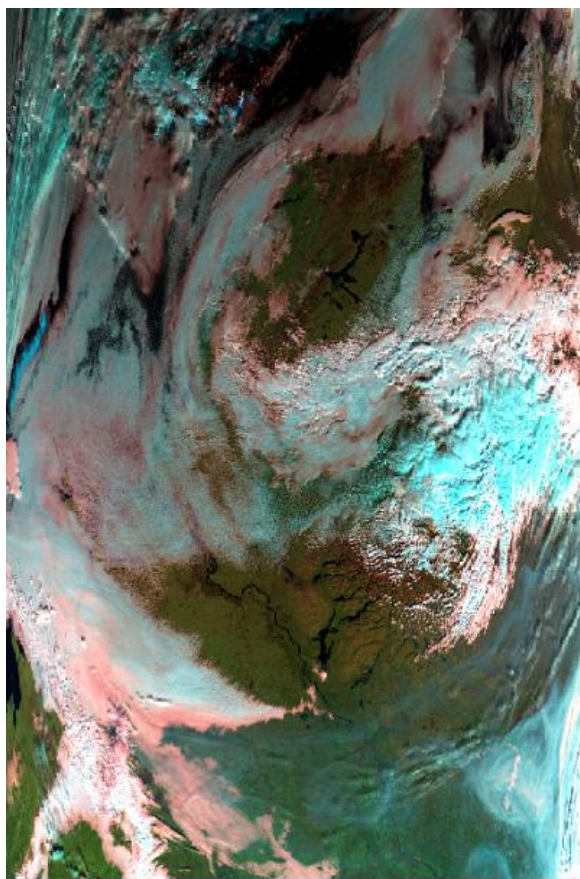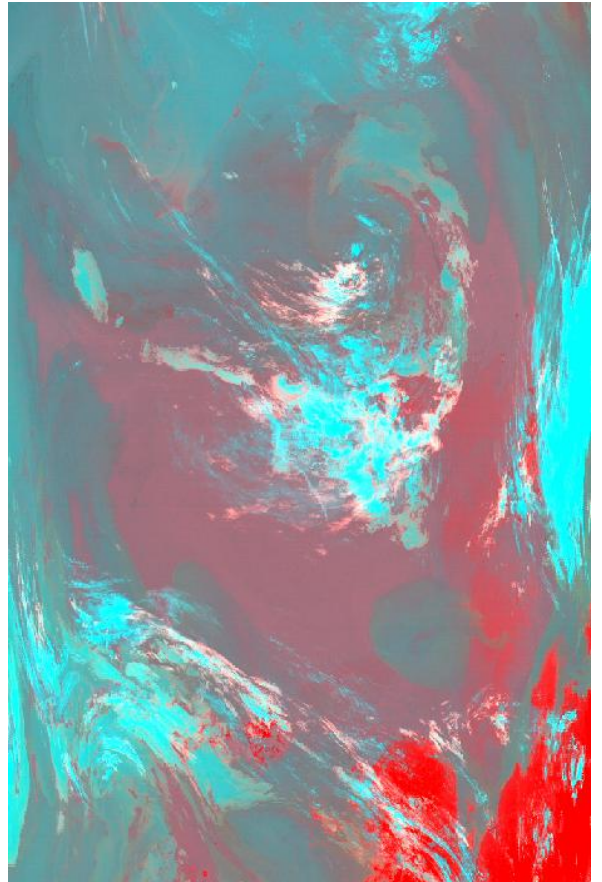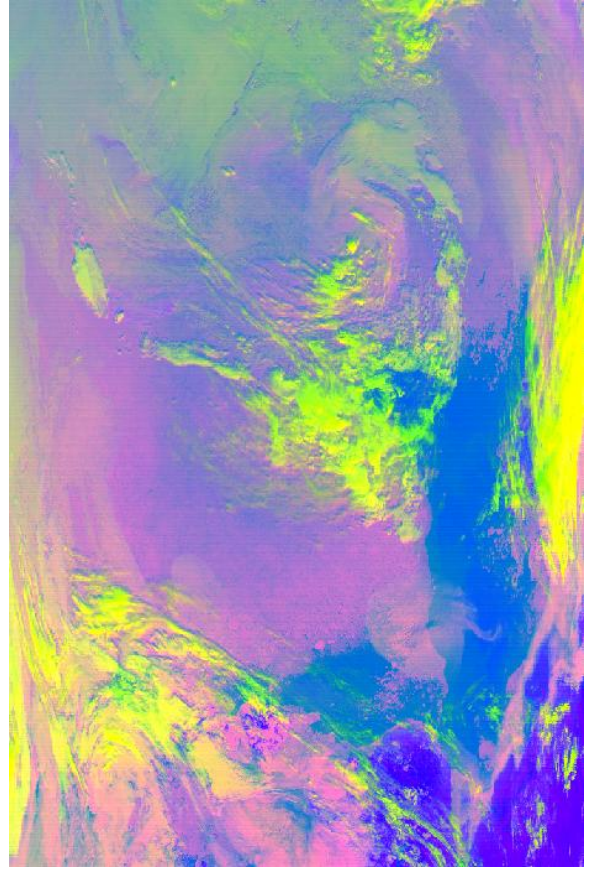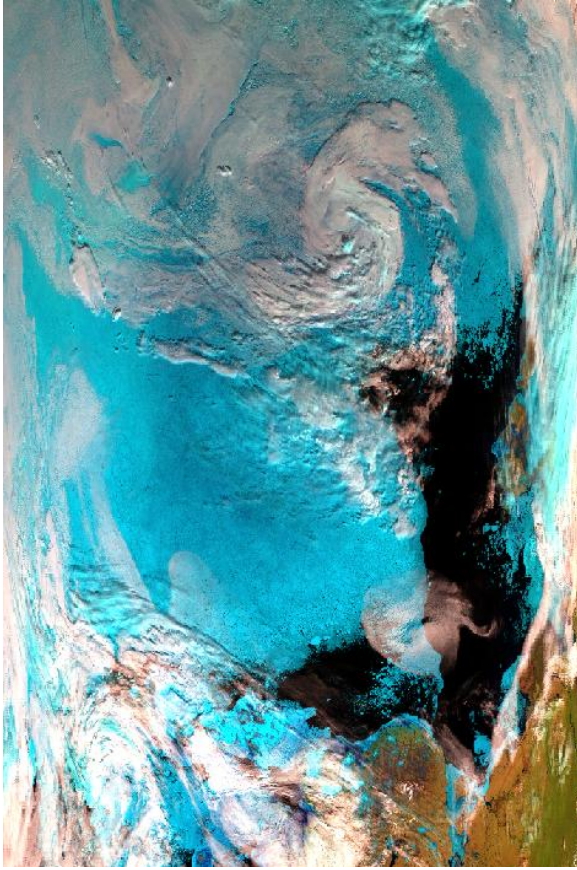
Satellite images after processing (20th of September 2016 9:10 UTC)